
Generalized Functional ANOVA in Closed-Form: A Unified View of Additive Explanations

Baptiste Ferrere*
EDF R&D, SINCLAIR Lab
Université de Toulouse

Nicolas Bousquet†
EDF R&D, SINCLAIR Lab
Sorbonne Université

Fabrice Gamboa†
Université de Toulouse, ANITI
Universidad Medellín

Jean-Michel Loubes†
Université de Toulouse, ANITI
INRIA Regalia

Abstract

The functional ANOVA, or Hoeffding decomposition, provides a principled framework for interpretability by decomposing a model prediction into main effects and higher-order interactions. For independent inputs, this classical decomposition is explicit. It is closely connected to SHAP values, generalized additive models, and orthogonal polynomial expansions, and therefore constitutes a fundamental tool for additive explainability. In the more general and realistic dependent setting, however, obtaining a tractable representation and estimating the decomposition from data remain challenging. In this work, we address this problem for continuous inputs. By combining Hilbert space methods with the generalized functional ANOVA, we build an explicit decomposition basis allowing to easily compute the decomposition. Our formulation recovers the classical independent case and its associated orthogonal decomposition. Building on this representation, we propose a simple but mighty algorithm to estimate the decomposition from a data sample in a model-agnostic setting and we compare it empirically with several state-of-the-art explanation methods, demonstrating the power of the approach.

1 Introduction

Modern machine-learning models perform thousands of nonlinear operations to produce their prediction, making the mapping between *inputs* and *outputs* often opaque to human inspection. This lack of interpretability has motivated several overlapping research areas: eXplainable AI (XAI), interpretability and trustworthy machine learning, which share the common goal of designing methods to explain the predictions of machine learning models. Existing approaches for XAI are typically grouped into three families: model-agnostic explanations, model-specific explanations, and inherently interpretable models. The first two are *post-hoc* methods, which aim to explain the predictions of an already trained model, most often a tree ensemble or a neural network in the tabular setting, from its inputs and outputs. Model-agnostic methods assume only access to the input–output behavior of the model, treating it as a *black box*, whereas model-specific methods exploit knowledge of its internal structure (e.g., trees, layers, or gradients). The third family constrains the model class itself so that predictions admit a direct interpretation by design. Despite their popularity, many of these approaches face two recurring criticisms. First, they often rely on *heuristic* constructions rather than rigorous representation theorems, making it difficult to characterize what the resulting explanations

*Correspondence to: Baptiste Ferrere <baptiste.ferrere@edf.fr>

†Equal supervising.

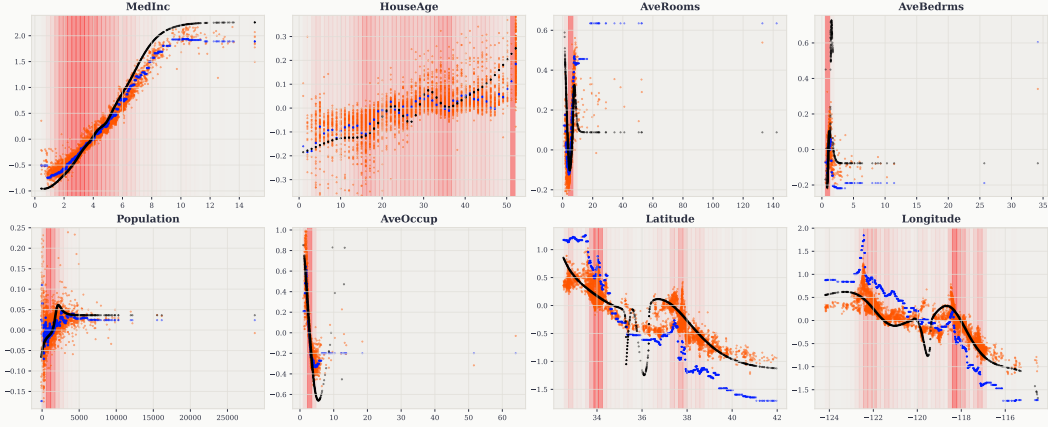


Figure 1: Estimated main effects on *California Housing*: our method (black) vs **TreeHFD** (main effects) and **TreeSHAP** on a trained XGB.

actually quantify. Second, they are frequently computationally expensive, and in some cases formally intractable.

However, these constructions are in fact closely connected to functional decompositions of the predictor. Highlighting this connection has two important consequences. First, it places additive explanations on rigorous footing: rather than isolated heuristics justified only by desirable axioms, they can be recognized as components of a well defined mathematical object, inheriting its structural properties. Second, it yields a unifying perspective in which many of the methods that pervade the explainability literature can be recast, compared, and analyzed on common ground. While variable importance captures only partial information about the input–output relationship, functional decompositions go further by expressing the predictor as a sum of interpretable components of increasing complexity, providing both feature importance and interaction. Several such decompositions exist, and different choices may lead to distinct interpretations of the same predictor. In this work, we carefully study the generalized functional ANOVA decomposition and its properties, which are particularly well-suited to additive explainability.

Outline of contributions.

1. We show that the generalized functional ANOVA decomposition [27] admits an explicit closed-form solution for continuous bounded features. As a direct consequence, the underlying non-parametric optimization problem reduces to a least-squares regression. Our formulation naturally recovers the well-known independent setting and the connections with Shapley values and orthogonal polynomials.
2. We derive an elementary estimation method that operates from a data sample and requires no access to the model’s internal structure. The resulting algorithm is purely **model-agnostic**, runs in **polynomial time**, and exploits the **sparsity** of the decomposition to remain tractable in practice. Fig 6 illustrates its *architecture* and Tab 2 shows its computational performances.
3. We conduct experiments on both synthetic and real-world datasets, comparing our estimator to several explanation methods and interpretable models. Our results clearly show that these methods are closely connected to specific components of the functional ANOVA decomposition, reinforcing the view that our framework unifies post-hoc explanation methods (see Figs 1,2,3) and interpretable models (see Fig 4).

2 Related Work

In the tabular setting, additive explanations have become overwhelmingly dominant, largely due to the success of SHapley Additive exPlanations, which unified a wide range of attribution methods and popularized additive explainability at scale. Beyond pure feature attribution, Shapley-based methods have since drawn on ideas from generalized additive models to incorporate interactions

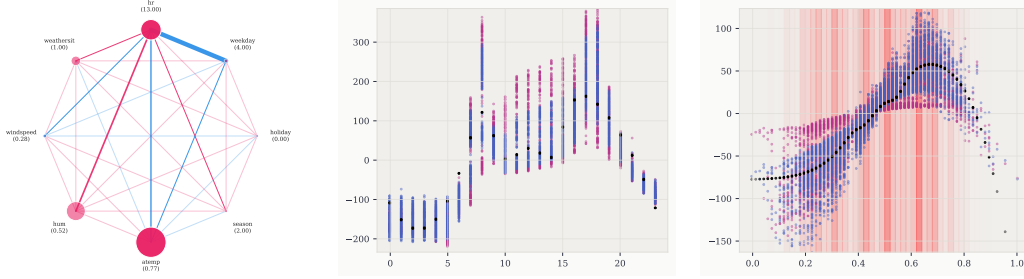


Figure 2: Decomposition of a trained MLP on *Bike Sharing*. *Left*: Network plot for a random instance of the dataset for visualizing local feature attribution and interaction. *Middle & Right*: For the features *hour* and *atemp* our method (black) vs *KernelSHAP* and *DeepSHAP*.

and higher-order effects, producing richer decompositions of the predictor. In parallel, generalized additive models themselves have long been used to build inherently interpretable predictors, from classical formulations to recent neural network and tree ensembles. Underlying both lines of work is a classical statistical object: the functional ANOVA decomposition, which, under suitable conditions and even in the presence of dependence, yields a unique additive functional representation of the predictor.

Shapley values. Originally introduced in cooperative game theory [33], Shapley values [52] were later imported into global sensitivity analysis [42, 43] and brought into machine learning [56], primarily through SHAP, which subsumes several post-hoc explanation methods such as LIME [50], DeepLIFT [53], and Layer-wise Relevance Propagation [5]. For tree ensembles, TreeSHAP [35] computes SHAP values in polynomial time, making them the standard explanation tool for tree-based models [2, 39, 6]. Beyond attribution, several works have connected Shapley values to functional decompositions of machine learning models [8, 24, 25, 38, 6]. However, all such approaches inherit both the estimation difficulties of Shapley values and the criticisms concerning their heuristic design and lack of theoretical justification [31].

Interpretable models. Generalized Additive Models (GAMs) [23] are among the most established interpretable model classes, restricting the predictor to a sum of univariate functions of the input features. This additive structure ensures that each component can be visualized and interpreted independently. Several modern variants have been proposed to improve predictive accuracy while preserving interpretability: GA^2M [34] extends GAMs with pairwise interactions, later scaled up in the Explainable Boosting Machine (EBM) [41] through cyclic gradient boosting; GAMI-Net [61] learns main effects and pairwise interactions through a structured neural architecture; Neural Additive Models (NAM) [1] and Neural Basis Models (NBM) [47] parameterize each component with an individual neural network; and NODE-GAM [11] builds on neural oblivious decision ensembles [46] to combine the flexibility of deep learning with the additive structure of GAMs.

Functional ANOVA. The functional ANOVA decomposition was first introduced by [26] for independent random variables, resulting in a unique orthogonal decomposition. [55] studied its properties under mild regularity conditions and [27] generalized the framework to dependent inputs. [12] and [28] further extended the validity of the decomposition to broader dependence structures, while [48] derived a coupled formulation together with a constructive approximation strategy in this dependent setting. On the estimation side, [32] proposed *pure interaction effects* for tree ensembles but requires knowledge of the input density, while [6] introduced TreeHFD, an efficient algorithm that operates directly from data; however, both approaches are restricted to tree-based models. In a related direction, [3] proposed Accumulated Local Effects (ALE), a visualization method closely connected to the functional ANOVA framework, though it addresses a slightly different problem. Very recently, [18] proposed an explicit solution to the problem formulated by [27] using the *inverse likelihood weighting* mechanism, but this work is restricted to categorical data.

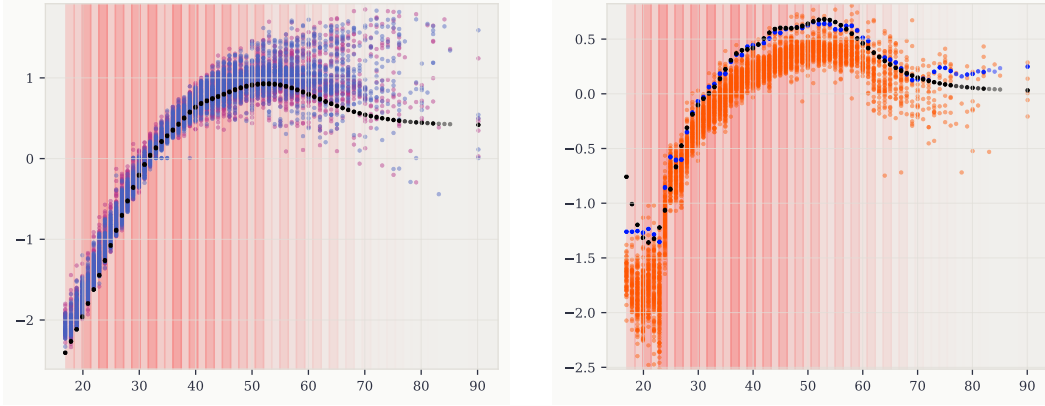


Figure 3: Estimated main effects for Age on *Census Income*. *Left*: Our method (black) vs **KernelSHAP** and **DeepSHAP** on a trained MLP. *Right*: Our method (black) vs **TreeHFD (main effects)** and **TreeSHAP** on a trained XGB.

3 Background

The Functional ANOVA decomposition provides a mathematical framework for decomposing a real-valued square integrable function $\nu(\mathbf{X})$ into a sum of components of increasing order:

$$\nu(\mathbf{X}) = \nu_\emptyset + \sum_{i=1}^p \nu_i(\mathbf{X}_i) + \sum_{i<j} \nu_{i,j}(\mathbf{X}_i, \mathbf{X}_j) + \dots = \sum_{S \subseteq [p]} \nu_S(\mathbf{X}_S), \quad (1)$$

where $\mathbf{X} := (\mathbf{X}_1, \dots, \mathbf{X}_p)$, $[p] := \{1, \dots, p\}$ and each component $\nu_S(\mathbf{X}_S)$ depends only on the subset of variables $\mathbf{X}_S := (\mathbf{X}_i)_{i \in S}$. The constant term ν_\emptyset captures the overall mean effect, the functions ν_i represent the marginal effects, and higher-order terms ν_S with $|S| \geq 2$ encode the pure interaction effects among the variables indexed by S . In this paper, we assume that \mathbf{X} has a joint density f with respect to the Lebesgue measure λ .

Generalized functional ANOVA [27]. For all $S \subseteq [p]$, let L_S^2 be the Hilbert space of square integrable functions of \mathbf{X}_S . One can define the components of (1) as the solution of the following optimization problem:

$$\{\nu_S\}_{S \subseteq [p]} := \operatorname{argmin}_{\{g_S \in L_S^2\}_{S \subseteq [p]}} \int_{\mathbb{R}^p} \left(\sum_{S \subseteq [p]} g_S(\mathbf{x}_S) - \nu(\mathbf{x}) \right)^2 f(\mathbf{x}) dx, \quad (2)$$

subject to the *hierarchical orthogonality constraint*:

$$\forall T \subsetneq S \subseteq [p], \forall g_T \in L_T^2, \int_{\mathbb{R}^p} \nu_S(\mathbf{x}_S) g_T(\mathbf{x}_T) f(\mathbf{x}) dx = 0. \quad (3)$$

Conceptually, decomposition (1) is sought under the constraint that information is non-redundant: for any subset $T \subseteq [p]$, the contribution of ν_S for $T \subsetneq S \subseteq [p]$ must capture only the variance that cannot be explained by any function of a strict subset of its variables \mathbf{X}_T . Roughly speaking, each component ν_S is *purely an $|S|$ -th order effect*, free of any lower-order information.

Under mild non-degeneracy conditions on the joint distribution [12, 28], the optimization problem (2) under the constraint (3) admits a unique solution, and the resulting decomposition generally allocates less variance to higher-order components. Throughout this work, we assume that the support of \mathbf{X} is a hyperrectangle and impose the following regularity condition on the density [55]:

Assumption 3.1. Without loss of generality, we assume that \mathbf{X} is supported on $[-1, 1]^p$ and that its density f is bounded away from zero and infinity: there exist constants $0 < c_1 < c_2$ such that:

$$\forall \mathbf{x} \in [-1, 1]^p, c_1 \leq f(\mathbf{x}) \leq c_2 < \infty. \quad (4)$$

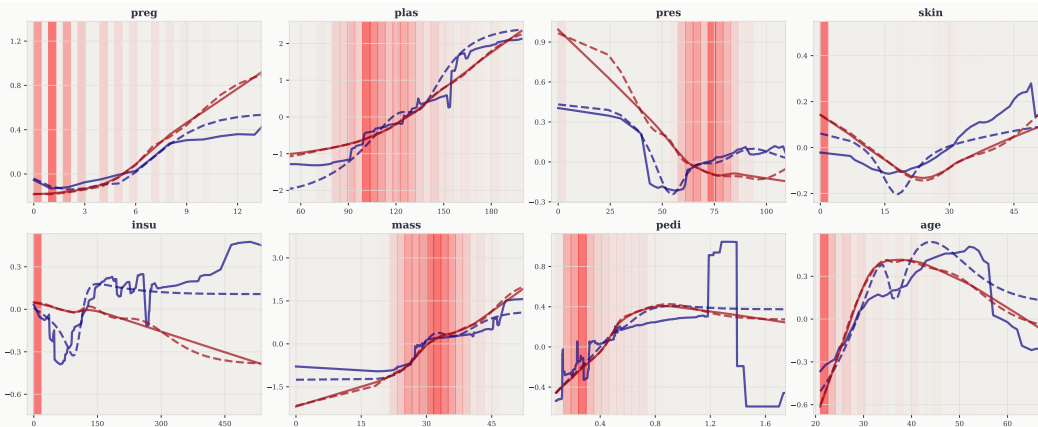


Figure 4: Comparison of native main effects from an EBM and a NAM with those recovered by our method on *Diabetes*. EBM (solid) vs our method (dashed); NAM (solid) vs our method (dashed).

Throughout the paper, we denote by $L^2 := L^2([-1, 1]^p, \mu_f)$ the Hilbert space of square-integrable functions on $[-1, 1]^p$ with respect to the measure $\mu_f := f\lambda$, endowed with the inner product $\langle g, h \rangle := \mathbb{E}[g(\mathbf{X})h(\mathbf{X})] = \int g(\mathbf{x})h(\mathbf{x})f(\mathbf{x})d\mathbf{x}$.

Theorem 3.2 ([55, 27]). *For any function ν member of L^2 , there exists a unique collection of functions $\{\nu_S\}_{S \subseteq [p]}$ such that $\nu(\mathbf{X}) = \sum_{S \subseteq [p]} \nu_S(\mathbf{X}_S)$ under the hierarchical orthogonality constraint (3).*

Independent setting. If the input variables are assumed to be mutually independent, *i.e.* the joint density f is the product of the marginal densities, then the components $\nu_S(\mathbf{X}_S)$ are explicit and are given by the Möbius transform [51] of the conditional expectations:

$$\forall S \subseteq [p], \nu_S(\mathbf{X}_S) = \sum_{T \subseteq S} (-1)^{|S|-|T|} \mathbb{E}[\nu(\mathbf{X}) \mid \mathbf{X}_T]. \quad (5)$$

In this particular setting, constraint (3) implies the mutual orthogonality of the decomposition:

$$\forall S, T \subseteq [p], S \neq T \implies \mathbb{E}[\nu_S(\mathbf{X}_S) \nu_T(\mathbf{X}_T)] = 0, \quad (6)$$

recovering the well-known orthogonal variance decomposition.

Remark 3.3 (Shapley values). A direct connection between the functional ANOVA decomposition and the Shapley formulation arises via Harsanyi dividends [22]. Let w be a set function on $[p]$, and define the associated value function v by $v(S) := \sum_{T \subseteq S} w(T)$ for all $S \subseteq [p]$. The Shapley value of player i in the cooperative game (p, v) then admits the closed-form expression $\phi_i = \sum_{S \ni i} \frac{w(S)}{|S|}$. Building on this identity, one can define, for any input \mathbf{x} , the *ANOVA based Shapley value* as the following local additive attribution: $\phi_i^{\text{ANOVA}}(\mathbf{x}) := \sum_{S \ni i} \frac{\nu_S(\mathbf{x}_S)}{|S|}$. Obviously, when the input features are mutually independent, this formulation coincides exactly with the standard SHAP values.

4 Main Result

In this section, we provide a **Riesz basis** [9] for L^2 satisfying the hierarchical orthogonality condition (3) and we will henceforth use *basis* to mean *Riesz basis*. Consequently, solving the optimization problem defined by [27] becomes a least squares regression problem. Finally, we provide an elementary algorithm to compute this decomposition from a data sample.

4.1 Decomposition basis

Throughout the paper, \mathbb{N}_+ denotes the set of positive integers. For each $m \in \mathbb{N}_+$, let \tilde{P}_m denote the normalized Legendre polynomial of degree m , whose definition and properties are recalled in Appendix A. In the next definition, we generalize the *inverse likelihood weighting mechanism*

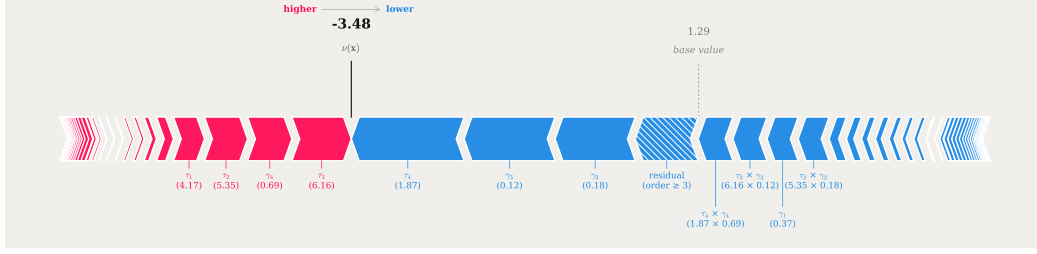


Figure 5: Force plot of **positive** and **negative** contributions (main effects, pair effects and residual) for a random instance of *Electrical Grid*.

[18] to continuous random variables. This mechanism will be the key tool to obtain hierarchical orthogonality. First, let $\xi_\emptyset := 1$.

Definition 4.1. For $S \subseteq [p]$, let denote f_S the marginal density of \mathbf{X}_S and define $\mathbf{m}_S := (m_j)_{j \in S} \in \mathbb{N}_+^{|S|}$. For $\mathbf{x} \in [-1, 1]^p$ we set

$$\xi_S^{(\mathbf{m}_S)}(\mathbf{x}) := \frac{1}{\sqrt{2^{p-|S|}}} \cdot \frac{\prod_{j \in S} \tilde{P}_{m_j}(\mathbf{x}_j)}{f_S(\mathbf{x}_S)} \quad (7)$$

We denote by Ξ the family of functions given by $\Xi := \left(\left(\xi_S^{(\mathbf{m}_S)} \right)_{\mathbf{m}_S \in \mathbb{N}_+^{|S|}} \right)_{S \subseteq [p]}$.

Theorem 4.2. *Let Assumption 3.1 hold. For any $\nu \in L^2$, there exists a unique family of coefficients $\mathbf{a} := (a_S^{(\mathbf{m}_S)})_{S \subseteq [p], \mathbf{m}_S \in \mathbb{N}_+^{|S|}}$ such that the unique components $(\nu_S)_{S \subseteq [p]}$ satisfying (2)–(3) admit the representation:*

$$\nu_S(\mathbf{X}_S) = \sum_{\mathbf{m}_S \in \mathbb{N}_+^{|S|}} a_S^{(\mathbf{m}_S)} \xi_S^{(\mathbf{m}_S)}(\mathbf{X}), \quad \forall S \subseteq [p]. \quad (8)$$

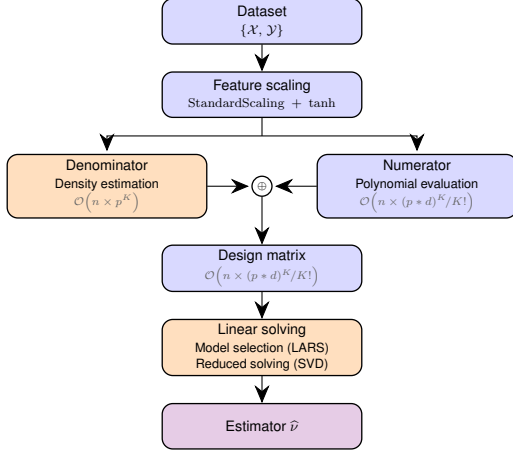
In particular, this provides the unique solution to the optimization problem formulated by [27] under Assumption 3.1.

As discussed before, under feature independence, the constraint (3) strengthens to full mutual orthogonality between components. In Appendix B (Proposition B.8), we show that the components derived from our formulation (8) indeed satisfy this stronger property in the independent case. In the particular case where $\mathbf{X}_1, \dots, \mathbf{X}_p$ are i.i.d. Uniform($[-1, 1]$), Ξ reduces to the tensorized normalized Legendre polynomials, which form an orthonormal basis of the L^2 space in this well known case.

4.2 Estimation

We assume an i.i.d. sample $\{\mathbf{X}^{(i)}\}_{i=1}^n$ is at hand together with the evaluations $\{\nu(\mathbf{X}^{(i)})\}_{i=1}^n$. Here, ν is treated as a *black-box* model: we can query it pointwise but have no access to its internal architecture (e.g., a trained neural network or tree ensemble). Since the basis Ξ is available in closed form, estimating the functional ANOVA decomposition reduces to estimating the coefficients

$$\mathbf{a} = \left(\left(a_S^{(\mathbf{m}_S)} \right)_{\mathbf{m}_S \in \mathbb{N}_+^{|S|}} \right)_{S \subseteq [p]}. \quad (9)$$



ID	Name	n	p
BS	Bike Sharing [17]	17 379	8
CH	California Housing [44]	20 640	8
CI	Census Income [30]	48 842	14
EG	Electrical Grid [4]	10 000	12
PI	Diabetes [54]	768	8
SC	Superconductivity [20]	21 263	81

Table 1: Datasets characteristics.

Figure 6: Illustration of our method to estimate the decomposition *from scratch* (see Appendix C).

A natural estimator is obtained by minimizing the empirical least-squares risk given by:

$$\mathcal{L}_n(\beta) := \sum_{i=1}^n \left(\nu(\mathbf{X}^{(i)}) - \sum_{S \subseteq [p]} \sum_{\mathbf{m}_S \in \mathbb{N}_+^{|S|}} \beta_S^{(\mathbf{m}_S)} \cdot \xi_S^{(\mathbf{m}_S)}(\mathbf{X}^{(i)}) \right)^2. \quad (10)$$

The parameter \mathbf{a} is however infinite-dimensional, as each multi-index \mathbf{m}_S ranges over $\mathbb{N}_+^{|S|}$, making the problem ill-posed without further structural assumptions. To make it tractable, we build on the polynomial chaos expansion literature [60, 7] and exploit two classical structural priors: the *sparsity-of-effects principle* [37], which posits that only a small number of effects drive the response, and the *reluctance principle* [62], which favors low-order effects over higher-order interactions at comparable explanatory power.

Definition 4.3 (Truncation set). Let $K \in [p]$ and $d \geq 1$ a positive integer. We define \mathcal{I}_K^d , the truncation set of *degree* d and *interaction order* K , as follows:

$$\mathcal{I}_K^d := \left\{ (S, \mathbf{m}_S) \mid S \subseteq [p] : |S| \leq K, \mathbf{m}_S \in \{1, \dots, d\}^{|S|} \right\}, \quad (11)$$

which contains exactly $N(p, K, d) := \sum_{k=0}^K \binom{p}{k} d^k$ elements.

Remark 4.4. A more general optimization problem could have been formulated by introducing a penalty $\Omega(\cdot)$ on the coefficients to be selected. We instead adopt the simplest approach and propose a twofold truncation, acting jointly on the interaction order and on the polynomial degrees. This choice is motivated by both computational and statistical considerations. First, the cardinality of \mathcal{I}_K^d grows as $\mathcal{O}((p * d)^K / K!)$, rendering high-order interactions rapidly intractable. Second, the *sparsity-of-effects principle* postulates that low-order effects dominate in most real-world systems. This intuition is further supported by the *reluctance principle*, which states that a main effect should be preferred over an interaction whenever both yield comparable predictive performance. Empirically, restricting the decomposition to main and pairwise effects is generally sufficient to recover black-box models with high fidelity, as consistently reported in the recent ANOVA and GAM/GA²M literature.

Restricting the empirical risk (10) to the truncated set \mathcal{I}_K^d yields a tractable estimator of the decomposition, defined as the solution of the finite-dimensional least-squares problem:

$$\hat{\mathbf{a}}_n^{K,d} := \operatorname{argmin}_{\beta \in \mathbb{R}^{N(p,K,d)}} \sum_{i=1}^n \left(\nu(\mathbf{X}^{(i)}) - \sum_{(S, \mathbf{m}_S) \in \mathcal{I}_K^d} \beta_S^{(\mathbf{m}_S)} \cdot \xi_S^{(\mathbf{m}_S)}(\mathbf{X}^{(i)}) \right)^2. \quad (12)$$

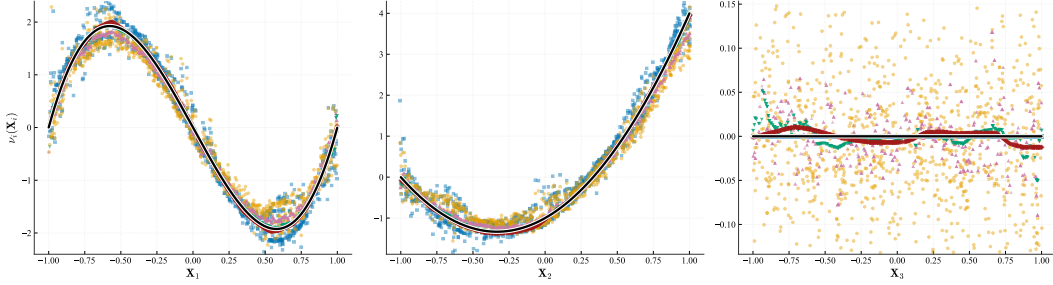


Figure 7: Estimated main effects in the analytical setting for \mathbf{X}_1 , \mathbf{X}_2 , and the irrelevant variable \mathbf{X}_3 . All methods (KernelSHAP, TreeSHAP, TreeHFD, NAM, EBM) closely track the **theoretical ANOVA component** on \mathbf{X}_1 and \mathbf{X}_2 , and correctly assign a near-zero contribution to \mathbf{X}_3 .

In theory, estimating the decomposition requires access to the marginal densities f_S ; in practice, we estimate these densities themselves using normalized Legendre polynomials. We illustrate the overall procedure in Fig 6 and defer a derivation of the full estimation pipeline in Appendix C.

5 Experiments

We first evaluate our framework on an analytical case. We instantiate the theoretical components in closed form and show that existing attribution methods implicitly approximate our formulation. We then conduct experiments on six real-world datasets. On each dataset, we train two predictive models of fixed architecture (a neural network and an XGBoost model) whose precise specifications are detailed in Appendix D. Our decomposition is applied to both and compared against several families of existing approaches, each paired with the model it is designed for. For neural networks, we compare against KernelSHAP, one of the most widely used model-agnostic explainability method, and its neural network specific counterpart DeepSHAP. For tree ensembles, we compare against TreeSHAP, the standard attribution method for tree-based models, as well as TreeHFD, which directly targets the functional ANOVA decomposition and provides an efficient implementation for XGBoost. Finally, to assess how our decomposition relates to intrinsically interpretable models, we train Neural Additive Models (NAM) and Explainable Boosting Machines (EBM), and compare the main effects natively produced by these architectures to those recovered by applying our decomposition to the same trained models.

Analytical case. We consider a random vector $\mathbf{X} \in [-1, 1]^3$ of following density

$$\forall \mathbf{x} \in [-1, 1]^3, \quad f_\rho(\mathbf{x}) := \frac{1}{8} (1 + \rho(\mathbf{x}_1\mathbf{x}_2 + \mathbf{x}_1\mathbf{x}_3 + \mathbf{x}_2\mathbf{x}_3)), \quad (13)$$

with $\rho \in (-1/3, 1)$ so that f_ρ satisfies Assumption 3.1. The target function is defined as

$$\nu(\mathbf{X}) := \nu_1(\mathbf{X}_1) + \nu_2(\mathbf{X}_2) + \nu_{1,2}(\mathbf{X}_1, \mathbf{X}_2), \quad (14)$$

whose components are given in closed form in Appendix D.4. This setting has two convenient features: the marginal and bivariate densities admit explicit expressions and the variable \mathbf{X}_3 is irrelevant to ν . This allows us to check if different methods correctly assign it a zero contribution. We display these theoretical components and the corresponding contributions given by the post-hoc explanation methods and interpretable models in Fig 7.

Real-world datasets. We evaluate our method on six publicly available datasets which span a variety of domains, sample sizes, and feature dimensionalities, covering both classification and regression tasks. Datasets characteristics are summarized in Tab 1 and the performance of our method to estimate the functional ANOVA are summarized in Tab 3.

The formal definition of all performance metrics are given in Appendix D. Briefly, Perf quantifies the predictive performance of the machine learning model; $K \in \{1, 2\}$ is the truncation level of our decomposition; R^2 is the reconstruction coefficient of determination of our estimator; and MaxCorr is a cosine-based quantity measuring the *worst* deviation from hierarchical orthogonality.

Table 2: Time (in s) to estimate the decomposition on the entire dataset (Mean \pm std over 10 repetitions).

ID	n	p	XGB	MLP	EBM	NAM
BS	17 379	8	9.806 \pm 0.228	5.741 \pm 0.182	9.721 \pm 0.206	–
CH	20 640	8	11.048 \pm 0.415	0.129 \pm 0.012	11.077 \pm 0.414	0.126 \pm 0.005
CI	48 842	14	0.575 \pm 0.023	0.597 \pm 0.053	0.691 \pm 0.010	–
EG	10 000	12	1.420 \pm 0.048	1.407 \pm 0.025	1.365 \pm 0.019	0.039 \pm 0.007
PI	768	8	0.237 \pm 0.006	0.230 \pm 0.009	0.230 \pm 0.006	0.013 \pm 0.001
SC	21 263	81	3.520 \pm 0.097	3.547 \pm 0.159	3.501 \pm 0.053	–

Table 3: Performance of our method across four model families.

Dataset	Model	Perf	K	R^2	MaxCorr	Dataset	Model	Perf	K	R^2	MaxCorr
BS (17 379, 8)	XGB	0.86	2	0.92	9.49e -2	EG (10 000, 12)	XGB	0.93	2	0.89	7.41e -3
	MLP	0.85	2	0.91	8.83e -2		MLP	0.98	2	0.95	6.61e -3
	EBM	0.83	2	0.96	9.52e -2		EBM	0.94	2	0.99	5.58e -3
	NAM	–	–	–	–		NAM	0.88	1	1.00	0.00
CH (20 640, 8)	XGB	0.84	2	0.86	6.35e -2	PI (768, 8)	XGB	0.74	2	0.85	9.56e -2
	MLP	0.81	1	0.88	0.00		MLP	0.73	2	0.99	0.00
	EBM	0.83	2	0.89	4.04e -2		EBM	0.76	2	0.97	0.00
	NAM	0.76	1	0.94	0.00		NAM	0.73	1	1.00	0.00
CI (48 842, 14)	XGB	0.88	1	0.91	0.00	SC (21 263, 81)	XGB	0.93	1	0.86	0.00
	MLP	0.85	1	0.94	0.00		MLP	0.91	1	0.89	0.00
	EBM	0.88	1	0.90	0.00		EBM	0.90	1	0.88	0.00
	NAM	–	–	–	–		NAM	–	–	–	–

Results. Our method yields highly accurate reconstructions across all four model families, with $R^2 \geq 0.85$ on every dataset. The systematically low interaction orders ($K \leq 2$) confirm the predominantly additive structure of these models and the sparsity of the *true* underlying decomposition. Despite the coarse plug-in estimation of the marginal densities, the hierarchical orthogonality between components is faithfully preserved. Finally, Tab 2 shows that our estimator is ultra fast in practice, while being model agnostic.

6 Discussion

Conclusion. We provided an explicit decomposition basis for the generalized functional ANOVA of continuous bounded random variables. Our formulation recovers classical orthogonal decompositions and their known connections with Shapley values and orthogonal polynomials. On the practical side, we proposed an elementary estimator that recovers the functional ANOVA from a data sample by solving a single linear system. Empirically, we compared our framework to state-of-the-art explanation methods and interpretable models for tabular data. We showed that these methods are closely related to the functional ANOVA, reinforcing that our framework offers a unifying perspective on additive explanations. Finally, our proposed approach to estimate the decomposition is very efficient and provides ultra fast explanations.

Limitations. We discuss the limitations of this paper in detail in Appendix F.

Future Work. Beyond strictly solving the limitations, our theoretical results open several promising directions. First extending the framework beyond bounded continuous distributions is a natural but non-trivial challenge. Handling mixed continuous-categorical inputs raises additional structural questions, as the decomposition would need to combine polynomial expansions with discrete summation over categorical levels. Second, incorporating a general penalization term into the theoretical least-squares risk would yield a tighter, possibly adaptive and/or minimax-optimal, estimator of the decomposition and connect our analysis to the broader model selection literature. Third, the explicit functional nature of the decomposition could yield new diagnostics on the geometry of black-box models. Finally, the uniqueness of this decomposition suggests that one may derive from it a *functional alignment* between the *real phenomenon* and the machine learning model.

Acknowledgments and Disclosure of Funding

The authors thank Joseph Muré (EDF R&D) for his careful reading and valuable comments. This work was partially supported by the French *Association Nationale de la Recherche et de la Technologie* (ANRT) through a CIFRE PhD project at Électricité de France (EDF). Fabrice Gamboa and Jean-Michel Loubes acknowledge support from the ANR-3IA Artificial and Natural Intelligence Toulouse Institute (ANITI).

References

- [1] Agarwal, R., Melnick, L., Frosst, N., Zhang, X., Lengerich, B., Caruana, R., and Hinton, G. E. (2021). Neural additive models: Interpretable machine learning with neural nets. *Advances in neural information processing systems*, 34:4699–4711.
- [2] Amoukou, S. I., Salaün, T., and Brunel, N. (2022). Accurate Shapley values for explaining tree-based models. In *International conference on artificial intelligence and statistics*, pages 2448–2465. PMLR.
- [3] Apley, D. W. and Zhu, J. (2020). Visualizing the effects of predictor variables in black box supervised learning models. *Journal of the Royal Statistical Society Series B: Statistical Methodology*, 82(4):1059–1086.
- [4] Arzamasov, V., Böhm, K., and Jochem, P. (2018). Towards concise models of grid stability. In *2018 IEEE international conference on communications, control, and computing technologies for smart grids (SmartGridComm)*, pages 1–6. IEEE.
- [5] Bach, S., Binder, A., Montavon, G., Klauschen, F., Müller, K.-R., and Samek, W. (2015). On pixel-wise explanations for non-linear classifier decisions by layer-wise relevance propagation. *PloS one*, 10(7):e0130140.
- [6] Bénard, C. (2025). Tree Ensemble Explainability through the Hoeffding Functional Decomposition and TreeHFD Algorithm. *Advances in Neural Information Processing Systems*.
- [7] Blatman, G. and Sudret, B. (2011). Adaptive sparse polynomial chaos expansion based on least angle regression. *Journal of computational Physics*, 230(6):2345–2367.
- [8] Bordt, S. and von Luxburg, U. (2023). From Shapley values to generalized additive models and back. In *International Conference on Artificial Intelligence and Statistics*, pages 709–745. PMLR.
- [9] Brézis, H. (2011). *Functional analysis, Sobolev spaces and partial differential equations*, volume 2. Springer.
- [10] Cencov, N. N. (1962). Estimation of an unknown distribution density from observations. *Soviet Math.*, 3:1559–1566.
- [11] Chang, C.-H., Caruana, R., and Goldenberg, A. (2021). NODE-GAM: Neural generalized additive model for interpretable deep learning. *arXiv:2106.01613*.
- [12] Chastaing, G., Gamboa, F., and Prieur, C. (2012). Generalized Hoeffding-Sobol Decomposition for Dependent Variables – Application to Sensitivity Analysis. *Electronic Journal of Statistics*, 6:2420–2448.
- [13] Chen, T., He, T., Benesty, M., Khotilovich, V., Tang, Y., Cho, H., Chen, K., Mitchell, R., Cano, I., Zhou, T., et al. (2015). Xgboost: extreme gradient boosting. *R package version 0.4-2*, 1(4):1–4.
- [14] Courant, R. and Hilbert, D. (2024). *Methods of mathematical physics, volume 2*. John Wiley & Sons.
- [15] Dua, D., Graff, C., et al. (2017). Uci machine learning repository, 2017. URL <http://archive.ics.uci.edu/ml>, 7(1):62.
- [16] Efron, B., Hastie, T., Johnstone, I., and Tibshirani, R. (2004). Least angle regression. *The Annals of Statistics*, 32(2).

- [17] Fanaee-T, H. and Gama, J. (2014). Event labeling combining ensemble detectors and background knowledge. *Progress in Artificial Intelligence*, 2(2):113–127.
- [18] Ferrere, B., Bousquet, N., Gamboa, F., Loubes, J.-M., and Muré, J. (2026). Exact Functional ANOVA Decomposition for Categorical Inputs Models. *arXiv:2603.02673*.
- [19] Ghanem, R. G. and Spanos, P. D. (2003). *Stochastic finite elements: a spectral approach*. Courier Corporation.
- [20] Hamidieh, K. (2018). A data-driven statistical model for predicting the critical temperature of a superconductor. *Computational Materials Science*, 154:346–354.
- [21] Harris, C. R., Millman, K. J., Van Der Walt, S. J., Gommers, R., Virtanen, P., Cournapeau, D., Wieser, E., Taylor, J., Berg, S., Smith, N. J., et al. (2020). Array programming with NumPy. *Nature*, 585(7825):357–362.
- [22] Harsanyi, J. C. (1963). A Simplified Bargaining Model for the n -Person Cooperative Game. *International Economic Review*, 4(2):194–220.
- [23] Hastie, T. J. (2017). Generalized additive models. In *Statistical models in S*, pages 249–307. Routledge.
- [24] Herren, A. and Hahn, P. R. (2022). Statistical aspects of SHAP: Functional ANOVA for model interpretation. *arXiv:2208.09970*.
- [25] Hiabu, M., Meyer, J. T., and Wright, M. N. (2023). Unifying local and global model explanations by functional decomposition of low dimensional structures. In *International conference on artificial intelligence and statistics*, pages 7040–7060. PMLR.
- [26] Hoeffding, W. (1948). A Class of Statistics with Asymptotically Normal Distribution. *The Annals of Mathematical Statistics*, 19(3):293–325.
- [27] Hooker, G. (2007). Generalized Functional ANOVA Diagnostics for High-Dimensional Functions of Dependent Variables. *Journal of Computational and Graphical Statistics*, 16(3):709–732.
- [28] Idrissi, M. I., Bousquet, N., Gamboa, F., Iooss, B., and Loubes, J.-M. (2025). Hoeffding decomposition of functions of random dependent variables. *Journal of Multivariate Analysis*, 208:105444.
- [29] Kingma, D. P. and Ba, J. (2014). Adam: A method for stochastic optimization. *arXiv preprint arXiv:1412.6980*.
- [30] Kohavi, R. et al. (1996). Scaling up the accuracy of naive-Bayes classifiers: A decision-tree hybrid. In *Kdd*, volume 96, pages 202–207.
- [31] Kumar, I. E., Venkatasubramanian, S., Scheidegger, C., and Friedler, S. (2020). Problems with Shapley-value-based explanations as feature importance measures. In *International conference on machine learning*, pages 5491–5500. PMLR.
- [32] Lengerich, B., Tan, S., Chang, C.-H., Hooker, G., and Caruana, R. (2020). Purifying interaction effects with the functional ANOVA: An efficient algorithm for recovering identifiable additive models. In *International Conference on Artificial Intelligence and Statistics*, pages 2402–2412. PMLR.
- [33] Lipovetsky, S. and Conklin, M. (2001). Analysis of regression in game theory approach. *Applied stochastic models in business and industry*, 17(4):319–330.
- [34] Lou, Y., Caruana, R., Gehrke, J., and Hooker, G. (2013). Accurate intelligible models with pairwise interactions. In *Proceedings of the 19th ACM SIGKDD international conference on Knowledge Discovery and Data mining*, pages 623–631.
- [35] Lundberg, S. M., Erion, G. G., and Lee, S.-I. (2018). Consistent individualized feature attribution for tree ensembles. *arXiv:1802.03888*.

- [36] Lundberg, S. M. and Lee, S.-I. (2017). A unified approach to interpreting model predictions. *Advances in neural information processing systems*, 30.
- [37] Montgomery, D. C. (2017). *Design and analysis of experiments*. John Wiley & Sons.
- [38] Muschalik, M., Baniecki, H., Fumagalli, F., Kolpaczki, P., Hammer, B., and Hüllermeier, E. (2024a). shapiq: Shapley interactions for machine learning. *Advances in Neural Information Processing Systems*, 37:130324–130357.
- [39] Muschalik, M., Fumagalli, F., Hammer, B., and Hüllermeier, E. (2024b). Beyond TreeSHAP: Efficient computation of any-order shapley interactions for tree ensembles. In *Proceedings of the AAAI Conference on Artificial Intelligence*, volume 38, pages 14388–14396.
- [40] Nelsen, R. B. (2006). *An introduction to copulas*. Springer.
- [41] Nori, H., Jenkins, S., Koch, P., and Caruana, R. (2019). InterpretML: A unified framework for machine learning interpretability. *arXiv preprint arXiv:1909.09223*.
- [42] Owen, A. B. (2014). Sobol’ indices and Shapley value. *SIAM/ASA Journal on Uncertainty Quantification*, 2(1):245–251.
- [43] Owen, A. B. and Prieur, C. (2017). On Shapley value for measuring importance of dependent inputs. *SIAM/ASA Journal on Uncertainty Quantification*, 5(1):986–1002.
- [44] Pace, R. K. and Barry, R. (1997). Sparse spatial autoregressions. *Statistics & Probability Letters*, 33(3):291–297.
- [45] Pedregosa, F., Varoquaux, G., Gramfort, A., Michel, V., Thirion, B., Grisel, O., Blondel, M., Prettenhofer, P., Weiss, R., Dubourg, V., et al. (2011). Scikit-learn: Machine learning in Python. *Journal of Machine Learning Research*, 12:2825–2830.
- [46] Popov, S., Morozov, S., and Babenko, A. (2019). Neural oblivious decision ensembles for deep learning on tabular data. *arXiv:1909.06312*.
- [47] Radenovic, F., Dubey, A., and Mahajan, D. (2022). Neural basis models for interpretability. *Advances in Neural Information Processing Systems*, 35:8414–8426.
- [48] Rahman, S. (2014). A generalized ANOVA dimensional decomposition for dependent probability measures. *SIAM/ASA Journal on Uncertainty Quantification*, 2(1):670–697.
- [49] Reed, M. and Simon, B. (1980). Volume 1: Functional analysis. In *Methods of Modern Mathematical Physics*. Elsevier.
- [50] Ribeiro, M. T., Singh, S., and Guestrin, C. (2016). "Why should I trust you?" Explaining the predictions of any classifier. In *Proceedings of the 22nd ACM SIGKDD international conference on Knowledge Discovery and Data mining*, pages 1135–1144.
- [51] Rota, G.-C. (1964). On the foundations of combinatorial theory: I. theory of Möbius functions. In *Classic Papers in Combinatorics*, pages 332–360. Springer.
- [52] Shapley, L. S. (1953). *A Value for n-Person Games*, pages 307–318. Princeton University Press, Princeton.
- [53] Shrikumar, A., Greenside, P., and Kundaje, A. (2017). Learning important features through propagating activation differences. In *International Conference on Machine Learning*, pages 3145–3153. PMLR.
- [54] Smith, J. W., Everhart, J. E., Dickson, W. C., Knowler, W. C., and Johannes, R. S. (1988). Using the adap learning algorithm to forecast the onset of diabetes mellitus. In *Proceedings of the Annual Symposium on Computer Application in Medical Care*, page 261.
- [55] Stone, C. J. (1994). The use of polynomial splines and their tensor products in multivariate function estimation. *The Annals of Statistics*, pages 118–171.

- [56] Sundararajan, M. and Najmi, A. (2020). The many Shapley values for model explanation. In *International Conference on Machine Learning*, pages 9269–9278. PMLR.
- [57] Szegő, G. (1939). *Orthogonal polynomials*, volume 23. American Mathematical Soc.
- [58] Tretter, C. (2008). *Spectral theory of block operator matrices and applications*. World Scientific.
- [59] Virtanen, P., Gommers, R., Oliphant, T. E., Haberland, M., Reddy, T., Cournapeau, D., Burovski, E., Peterson, P., Weckesser, W., Bright, J., et al. (2020). Scipy 1.0: fundamental algorithms for scientific computing in python. *Nature methods*, 17(3):261–272.
- [60] Xiu, D. and Karniadakis, G. E. (2002). The Wiener–Askey polynomial chaos for stochastic differential equations. *SIAM Journal on Scientific Computing*, 24(2):619–644.
- [61] Yang, Z., Zhang, A., and Sudjianto, A. (2021). GAMI-Net: An explainable neural network based on generalized additive models with structured interactions. *Pattern Recognition*, 120:108192.
- [62] Yu, G., Bien, J., and Tibshirani, R. (2019). Reluctant interaction modeling. *arXiv:1907.08414*.

A Legendre Polynomials

In this section, we rely on results that have been widely studied by [57].

Definition A.1. For any non-negative integer $m \in \mathbb{N}$, we denote by P_m the Legendre polynomial of degree m . This family is uniquely defined by the three-term recurrence relation:

$$\begin{cases} P_0(X) = 1, \\ P_1(X) = X, \\ (m+1)P_{m+1}(X) = (2m+1)XP_m(X) - mP_{m-1}(X), \quad \forall m \geq 1. \end{cases} \quad (15)$$

Proposition A.2. *The Legendre polynomials are mutually orthogonal and satisfy the following identity:*

$$\forall n, m \in \mathbb{N}, \quad \int_{-1}^1 P_n(x)P_m(x)dx = \frac{2}{2n+1} \mathbf{1}_{\{n=m\}}. \quad (16)$$

Definition A.3. For any integer $m \in \mathbb{N}$, we denote by \tilde{P}_m the normalized Legendre polynomial of degree m defined as:

$$\tilde{P}_m := \sqrt{\frac{2m+1}{2}} P_m. \quad (17)$$

Theorem A.4. [49, 19, 14] *For any $\alpha := (\alpha_1, \dots, \alpha_p) \in \mathbb{N}^p$, we define the following tensorized product of normalized Legendre polynomials:*

$$\Phi_\alpha(X_1, \dots, X_p) := \prod_{j=1}^p \tilde{P}_{\alpha_j}(X_j). \quad (18)$$

The collection $(\Phi_\alpha)_{\alpha \in \mathbb{N}^p}$ forms a Hilbert basis (i.e. an orthonormal basis) of $L^2([-1, 1]^p)$ equipped with the Lebesgue measure λ .

A direct consequence of the previous theorem is an ANOVA-type indexing of the Hilbert basis of $L^2([-1, 1]^p, \lambda)$, in which each basis element depends only on a prescribed subset of variables. Recall that \mathbb{N}_+ denotes the set of positive integers. For any $S \subseteq [p]$ and any $\mathbf{m}_S := (m_j)_{j \in S} \in \mathbb{N}_+^{|S|}$, set

$$\psi_S^{(\mathbf{m}_S)} := \frac{1}{\sqrt{2^{p-|S|}}} \prod_{j \in S} \tilde{P}_{m_j}, \quad (19)$$

with the convention $\psi_\emptyset := 1/\sqrt{2^p}$. Then the family

$$\left\{ \psi_S^{(\mathbf{m}_S)} : S \subseteq [p], \mathbf{m}_S \in \mathbb{N}_+^{|S|} \right\} \quad (20)$$

is a Hilbert basis of $L^2([-1, 1]^p, \lambda)$. Indeed, for any $\alpha \in \mathbb{N}^p$, let $S_\alpha := \{j \in [p] : \alpha_j > 0\}$ denote its support and $\alpha_{S_\alpha} \in \mathbb{N}_+^{|S_\alpha|}$ its restriction to the nonzero coordinates. Since $\tilde{P}_0 = 1/\sqrt{2}$, one has

$$\Phi_\alpha = \prod_{j=1}^p \tilde{P}_{\alpha_j} = \frac{1}{\sqrt{2^{p-|S_\alpha|}}} \prod_{j \in S_\alpha} \tilde{P}_{\alpha_j} = \psi_{S_\alpha}^{(\alpha_{S_\alpha})}. \quad (21)$$

Moreover, the map

$$\alpha \in \mathbb{N}^p \longmapsto (S_\alpha, \alpha_{S_\alpha}) \in \bigsqcup_{S \subseteq [p]} \mathbb{N}_+^{|S|}$$

is a bijection, and the result follows by reindexing $(\Phi_\alpha)_{\alpha \in \mathbb{N}^p}$ along it.

Remark A.5. A key consequence of the orthogonality of the basis is the orthogonality to the constant:

$$\forall S \subseteq [p] \setminus \emptyset, \forall \mathbf{m}_S \in \mathbb{N}_+^{|S|}, \quad \int_{[-1, 1]^p} \psi_S^{(\mathbf{m}_S)}(\mathbf{x}) d\lambda(\mathbf{x}) = 0. \quad (22)$$

B Proofs

The proof of Theorem 4.2 proceeds as follows. We first show that the spaces $L^2([-1, 1]^p, \lambda)$ and $L^2([-1, 1]^p, \mu_f)$ are norm-equivalent (see Lemma B.1). Consequently, rather than establishing that Ξ is a basis of $L^2([-1, 1]^p, \mu_f)$, it suffices to show that Ξ is a basis of $L^2([-1, 1]^p, \lambda)$. Accordingly, Definition B.2 and Propositions B.3, B.4, and B.6 are stated in the space $L^2([-1, 1]^p, \lambda)$. By means of a suitably chosen operator \mathcal{T} , we show that Ξ is a Riesz basis of $L^2([-1, 1]^p, \lambda)$, and therefore a Riesz basis of $L^2([-1, 1]^p, \mu_f)$. The hierarchical orthogonality property (see Proposition B.7) is naturally established in $L^2([-1, 1]^p, \mu_f)$. Combining these results yields the proof of the theorem.

Lemma B.1. *Let f be a probability density with respect to the Lebesgue measure λ on $[-1, 1]^p$, and assume that there exist constants $0 < c_1 \leq c_2 < \infty$ such that*

$$\forall \mathbf{x} \in [-1, 1]^p, \quad c_1 \leq f(\mathbf{x}) \leq c_2 \quad (23)$$

The spaces $L^2([-1, 1]^p, \lambda)$ and $L^2([-1, 1]^p, \mu_f)$ coincide as sets, and their norms are equivalent: for every measurable function g ,

$$c_1 \|g\|_{L^2(\lambda)}^2 \leq \|g\|_{L^2(\mu_f)}^2 \leq c_2 \|g\|_{L^2(\lambda)}^2. \quad (24)$$

Proof. Let $g : [-1, 1]^p \rightarrow \mathbb{R}$ be a measurable function. By definition of μ_f one has:

$$\|g\|_{L^2(\mu_f)}^2 = \int_{[-1, 1]^p} g(\mathbf{x})^2 d\mu_f(\mathbf{x}) = \int_{[-1, 1]^p} g(\mathbf{x})^2 f(\mathbf{x}) d\lambda(\mathbf{x}). \quad (25)$$

Using equation (23), we obtain:

$$c_1 \int_{[-1, 1]^p} g(\mathbf{x})^2 d\lambda(\mathbf{x}) \leq \int_{[-1, 1]^p} g(\mathbf{x})^2 f(\mathbf{x}) d\lambda(\mathbf{x}) \leq c_2 \int_{[-1, 1]^p} g(\mathbf{x})^2 d\lambda(\mathbf{x}),$$

which finally gives the norm equivalence. This implies that the two spaces have the same Cauchy sequences. \square

Definition B.2. For every set $S \subseteq [p]$, let Π_S be the orthogonal projection onto

$$V_S := \overline{\text{span}} \left\{ \psi_S^{(\mathbf{m}_S)} \mid \mathbf{m}_S \in \mathbb{N}_+^{|S|} \right\}, \quad (26)$$

where $\overline{\text{span}}$ denotes the closure of the linear span in $L^2([-1, 1]^p, \lambda)$. Let also $\{w_S\}_{S \subseteq [p]}$ be a given collection of measurable functions, satisfying for all $S \subseteq [p]$ and all $\mathbf{x}_S \in [-1, 1]^{|S|}$:

$$0 < \kappa_1 \leq w_S(\mathbf{x}_S) \leq \kappa_2 < \infty, \quad (27)$$

for a given couple of positive constants $0 < \kappa_1 \leq \kappa_2 < \infty$. We define the operator \mathcal{T} as follows:

$$\mathcal{T} : \begin{cases} L^2([-1, 1]^p, \lambda) & \longrightarrow & L^2([-1, 1]^p, \lambda) \\ u & \longmapsto & \sum_{S \subseteq [p]} w_S \Pi_S(u), \end{cases} \quad (28)$$

Note that \mathcal{T} depends on the given collection of functions $\{w_S\}_{S \subseteq [p]}$ but we simply denote it by \mathcal{T} for simplicity.

Proposition B.3. *The operator \mathcal{T} is bounded.*

Proof. Using that $(\psi_S^{(\mathbf{m}_S)})_{S \subseteq [p], \mathbf{m}_S \in \mathbb{N}_+^{|S|}}$ is a Hilbert basis of $L^2([-1, 1]^p, \lambda)$, we have the orthogonal decomposition

$$L^2([-1, 1]^p, \lambda) = \bigoplus_{S \subseteq [p]}^\perp V_S. \quad (29)$$

Consequently, any $u \in L^2([-1, 1]^p, \lambda)$ admits the unique orthogonal decomposition

$$u = \sum_{S \subseteq [p]} u_S, \quad u_S := \Pi_S(u). \quad (30)$$

Let $u \in L^2([-1, 1]^p, \lambda)$, we have:

$$\|\mathcal{T}(u)\|_{L^2(\lambda)} = \left\| \sum_{S \subseteq [p]} w_S u_S \right\| \quad (31)$$

$$\leq \sum_{S \subseteq [p]} \|w_S u_S\| \quad (32)$$

$$\leq \kappa_2 \sum_{S \subseteq [p]} \|u_S\| \quad (33)$$

$$\leq \kappa_2 2^{p/2} \|u\| \quad (34)$$

which gives the desired result. \square

Proposition B.4. *The operator \mathcal{T} is invertible.*

Proof. For every $S, S' \subseteq [p]$, we define the following operator:

$$A_{S,S'} : \begin{cases} V_S & \longrightarrow V_{S'} \\ u_S & \longmapsto (\Pi_{S'} \circ \mathcal{T})(u_S) \end{cases} \quad (35)$$

We have the following identity for every $u \in L^2([-1, 1]^p, \lambda)$:

$$\mathcal{T}(u) = \sum_{S \subseteq [p]} \sum_{S' \subseteq [p]} A_{S,S'}(\Pi_S(u)). \quad (36)$$

We denote by $L_S^2([-1, 1]^{|S|}, \lambda)$ the Hilbert space of square-integrable functions depending only on the variables indexed by $S \subseteq [p]$. Observe that for every $S \subseteq [p]$, the operator \mathcal{T} leaves this space invariant, i.e.,

$$\mathcal{T} \left(L_S^2([-1, 1]^{|S|}, \lambda) \right) \subseteq L_S^2([-1, 1]^{|S|}, \lambda). \quad (37)$$

Indeed, let $S \subseteq [p]$, the space $L_S^2([-1, 1]^{|S|}, \lambda)$ admits the following orthogonal decomposition:

$$L_S^2([-1, 1]^{|S|}, \lambda) = \bigoplus_{T \subseteq S}^\perp V_T. \quad (38)$$

So for any $u \in L_S^2([-1, 1]^{|S|}, \lambda)$, u uniquely expresses as $u = \sum_{T \subseteq S} \Pi_T(u)$. By applying \mathcal{T} to this sum, we obtain:

$$\mathcal{T}(u) = \sum_{T \subseteq S} w_T \Pi_T(u), \quad (39)$$

which is obviously an element of $L_S^2([-1, 1]^{|S|}, \lambda)$. Furthermore, observe that we have the following decomposition:

$$L^2([-1, 1]^p, \lambda) = \underbrace{\bigoplus_{T \subseteq S}^\perp V_T}_{L_S^2([-1, 1]^{|S|}, \lambda)} \bigoplus \bigoplus_{S' \not\subseteq S}^\perp V_{S'} \quad (40)$$

A direct consequence of this stabilization property using the previous decomposition is:

$$\forall S, S' \subseteq [p], \quad S' \not\subseteq S \implies A_{S,S'} = 0, \quad (41)$$

Consequently, the operator matrix $\mathbf{A} := (A_{S,S'})_{S, S' \subseteq [p]}$ is triangular (an illustration in dimension 3 is provided in (51)). To show the invertibility of \mathcal{T} , it suffices to prove that all the diagonal blocks are invertible [58], indeed in any finite partially-ordered family of blocks where off-diagonal blocks vanish outside $S' \subseteq S$, invertibility follows by induction on $|S|$. Let $S \subseteq [p]$, we will show that

$A_{S,S}$ is invertible. First, $A_{S,S}$ is clearly a linear operator and so an endomorphism of V_S . Let take $u_S \in V_S$, we have:

$$\langle A_{S,S}(u_S), u_S \rangle = \langle (\Pi_S \circ \mathcal{T})(u_S), u_S \rangle \quad (42)$$

$$= \langle \Pi_S(w_S u_S), u_S \rangle \quad (43)$$

$$= \langle w_S u_S, \Pi_S^*(u_S) \rangle \quad (44)$$

$$= \langle w_S u_S, \Pi_S(u_S) \rangle \quad (45)$$

$$= \langle w_S u_S, u_S \rangle \quad (46)$$

$$= \int w_S u_S^2 d\lambda \quad (47)$$

$$\geq \kappa_1 \|u_S\|_{L^2(\lambda)}^2, \quad (48)$$

so the operator $A_{S,S}$ is *coercive*. A similar computation would show that the operator is *bounded*, i.e.

$$\forall u_S, v_S \in V_S, \quad |\langle A_{S,S}(u_S), v_S \rangle| \leq \kappa_2 \|u_S\|_{L^2(\lambda)} \|v_S\|_{L^2(\lambda)}. \quad (49)$$

Finally, by applying the Lax-Milgram theorem [9], we obtain that $A_{S,S}$ is invertible and the desired result. \square

Remark B.5. Let $p = 3$. We illustrate the triangular structure of the matrix \mathbf{A} and of the operator \mathcal{T} . Order the subsets of $[p]$ as follows:

$$\{\emptyset, \{1\}, \{2\}, \{3\}, \{1, 2\}, \{1, 3\}, \{2, 3\}, \{1, 2, 3\}\}. \quad (50)$$

The coefficient $A_{S,S'}(u_S)$ denotes the projection onto $V_{S'}$ of $w_S u_S$, which belongs to $L_S^2([-1, 1]^{|S|}, \lambda)$. In the case $p = 3$, the matrix takes the form

$$\begin{array}{c} \emptyset \\ \{1\} \\ \{2\} \\ \{3\} \\ \{1, 2\} \\ \{1, 3\} \\ \{2, 3\} \\ \{1, 2, 3\} \end{array} \begin{array}{c} \left[\begin{array}{cccccccc} * & & & & & & & \\ * & * & & & & & & \\ * & & * & & & & & \\ * & & & * & & & & \\ * & * & * & & * & & & \\ * & * & & * & & * & & \\ * & & * & * & & & * & \\ * & * & * & * & * & * & * & * \end{array} \right] \end{array} \quad (51)$$

where * indicates entries that are potentially non-zero.

Proposition B.6. \mathcal{T} is a linear homeomorphism of $L^2([-1, 1]^p, \lambda)$.

Proof. As a direct consequence of proposition B.3 and proposition B.4, \mathcal{T} is a bounded automorphism of $L^2([-1, 1]^p, \lambda)$. Using the Banach-Schauder theorem [9], \mathcal{T} is a homeomorphism. \square

Proposition B.7 (Hierarchical orthogonality). *The family Ξ satisfies the hierarchical orthogonality condition in $L^2([-1, 1]^p, \mu_f)$. More formally, we have:*

$$\forall T \subsetneq S \subseteq [p], \forall \mathbf{m}_S \in \mathbb{N}_+^{|S|}, \forall \mathbf{n}_T \in \mathbb{N}_+^{|T|}, \quad \mathbb{E} \left[\xi_S^{(\mathbf{m}_S)}(\mathbf{X}) \cdot \xi_T^{(\mathbf{n}_T)}(\mathbf{X}) \right] = 0. \quad (52)$$

In particular, all basis elements are centered, i.e.

$$\forall S \subseteq [p] \setminus \emptyset, \quad \mathbb{E} \left[\xi_S^{(\mathbf{m}_S)}(\mathbf{X}) \right] = 0. \quad (53)$$

Proof. Let us consider $T \subsetneq S \subseteq [p]$, $\mathbf{m}_S := (m_s)_{s \in S} \in \mathbb{N}_+^{|S|}$, $\mathbf{n}_T := (n_t)_{t \in T} \in \mathbb{N}_+^{|T|}$. For simplicity, we define $C := S \setminus T$ and consider $\mathbf{m}_C := (m_c)_{c \in C}$. We have:

$$\mathbb{E} \left[\xi_S^{(\mathbf{m}_S)}(\mathbf{X}) \cdot \xi_T^{(\mathbf{n}_T)}(\mathbf{X}) \right] = \int_{[-1,1]^p} \xi_S^{(\mathbf{m}_S)}(\mathbf{x}) \cdot \xi_T^{(\mathbf{n}_T)}(\mathbf{x}) \cdot f(\mathbf{x}) d\lambda(\mathbf{x}), \quad (54)$$

$$= \int_{[-1,1]^{|S|}} \xi_S^{(\mathbf{m}_S)}(\mathbf{x}) \cdot \xi_T^{(\mathbf{n}_T)}(\mathbf{x}) \cdot f_S(\mathbf{x}_S) d\lambda(\mathbf{x}_S), \quad (55)$$

$$\propto \int_{[-1,1]^{|S|}} \frac{\prod_{s \in S} \tilde{P}_{m_s}(\mathbf{x}_s)}{f_S(\mathbf{x}_S)} \frac{\prod_{t \in T} \tilde{P}_{n_t}(\mathbf{x}_t)}{f_T(\mathbf{x}_T)} f_S(\mathbf{x}_S) d\lambda(\mathbf{x}_S), \quad (56)$$

$$\propto \int_{[-1,1]^{|S|}} \prod_{s \in S} \tilde{P}_{m_s}(\mathbf{x}_s) \frac{\prod_{t \in T} \tilde{P}_{n_t}(\mathbf{x}_t)}{f_T(\mathbf{x}_T)} d\lambda(\mathbf{x}_S), \quad (57)$$

$$\propto \int_{[-1,1]^{|S|}} \underbrace{\prod_{c \in C} \tilde{P}_{m_c}(\mathbf{x}_c)}_{\sqrt{2^{p-|C|}} \psi_C^{(\mathbf{m}_C)}(\mathbf{x}_C)} \cdot \underbrace{\frac{\prod_{t \in T} \tilde{P}_{m_t}(\mathbf{x}_t) \tilde{P}_{n_t}(\mathbf{x}_t)}{f_T(\mathbf{x}_T)}}_{u(\mathbf{x}_T)} d\lambda(\mathbf{x}_S), \quad (58)$$

$$\propto \underbrace{\int_{[-1,1]^{|C|}} \psi_C^{(\mathbf{m}_C)}(\mathbf{x}_C) d\lambda(\mathbf{x}_C)}_{=0} \cdot \int_{[-1,1]^{|T|}} u(\mathbf{x}_T) d\lambda(\mathbf{x}_T), \quad (59)$$

$$= 0. \quad (60)$$

□

Proof of Theorem 4.2. First, observe that since $c_1 \leq f \leq c_2$, we have for all sets $S \subseteq [p]$:

$$c_1 2^{p-|S|} \leq f_S \leq c_2 2^{p-|S|}. \quad (61)$$

Consequently, a uniform bound for all f_S is given by:

$$c_1 \leq f_S \leq c_2 2^p. \quad (62)$$

Moreover, recall that our proposed collection of functions Ξ is given by:

$$\forall \mathbf{x} \in [-1,1]^p, \quad \Xi(\mathbf{x}) = \left(\left(\frac{\psi_S^{(\mathbf{m}_S)}(\mathbf{x})}{f_S(\mathbf{x}_S)} \right)_{\mathbf{m}_S \in \mathbb{N}_+^{|S|}} \right)_{S \subseteq [p]}. \quad (63)$$

In this case, we obviously have:

$$\forall S \subseteq [p], \forall \mathbf{m}_S \in \mathbb{N}_+^{|S|}, \quad \xi_S^{(\mathbf{m}_S)} = \mathcal{T}(\psi_S^{(\mathbf{m}_S)}), \quad (64)$$

by defining the weight functions w_S as follows: $w_S := 1/f_S$ with $\kappa_1 := 1/(c_2 2^p)$ and $\kappa_2 := 1/c_1$. Thanks to Proposition B.6, Ξ is the direct image of a Hilbert basis by a homeomorphism \mathcal{T} which implies that Ξ is a *Riesz basis* of $L^2([-1,1]^p, \lambda)$. In particular, by Lemma B.1 the family Ξ is also a Riesz basis of $L^2([-1,1]^p, \mu_f)$. As a direct consequence of this result, any function $\nu \in L^2([-1,1]^p, \mu_f)$ admits the following unique representation:

$$\nu(\mathbf{X}) = \sum_{S \subseteq [p]} \sum_{\mathbf{m}_S \in \mathbb{N}_+^{|S|}} a_S^{(\mathbf{m}_S)} \cdot \xi_S^{(\mathbf{m}_S)}(\mathbf{X}), \quad (65)$$

where $\mathbf{a} := (a_S^{(\mathbf{m}_S)})_{S \subseteq [p], \mathbf{m}_S \in \mathbb{N}_+^{|S|}}$ is a unique collection of real coefficients entirely determined by ν and f . For every $S \subseteq [p]$, the ANOVA components ν_S are naturally defined by:

$$\nu_S(\mathbf{X}_S) := \sum_{\mathbf{m}_S \in \mathbb{N}_+^{|S|}} a_S^{(\mathbf{m}_S)} \cdot \xi_S^{(\mathbf{m}_S)}(\mathbf{X}). \quad (66)$$

Furthermore, these components obviously satisfy the hierarchical orthogonality constraint (3), thanks to the proposition B.7. Finally, the representation given in the basis Ξ is the exact analytical solution to the problem formulated by [27]. □

Proposition B.8 (Recovering orthogonality). *When the components of \mathbf{X} are mutually independent, we have:*

$$\forall S, T \subseteq [p], \quad S \neq T \implies \mathbb{E}[\nu_S(\mathbf{X}_S) \cdot \nu_T(\mathbf{X}_T)] = 0. \quad (67)$$

Proof. To show that the resulting decomposition is mutually orthogonal by set, it suffices to prove that for any sets S, T such that $S \neq T$ and for any vector of indices $\mathbf{m}_S, \mathbf{n}_T$, one has:

$$\mathbb{E} \left[\xi_S^{(\mathbf{m}_S)}(\mathbf{X}) \cdot \xi_T^{(\mathbf{n}_T)}(\mathbf{X}) \right] = 0. \quad (68)$$

Under independence, the density expresses as the following product $f = f_1 \cdots f_p$. The elements of our basis becomes:

$$\forall S \subseteq [p], \forall \mathbf{m}_S \in \mathbb{N}_+^{|S|}, \quad \xi_S^{(\mathbf{m}_S)} = \frac{1}{\sqrt{2^{p-|S|}}} \cdot \prod_{j \in S} \frac{\tilde{P}_{m_j}}{f_j}. \quad (69)$$

Let $S \neq T \subseteq [p]$, without loss of generality, we fix $s^* \in S$ such that $s^* \notin T$. We have:

$$\mathbb{E} \left[\xi_S^{(\mathbf{m}_S)}(\mathbf{X}) \cdot \xi_T^{(\mathbf{n}_T)}(\mathbf{X}) \right] = \mathbb{E} \left[\frac{1}{\sqrt{2^{p-|S|}}} \prod_{s \in S} \frac{\tilde{P}_{m_s}(\mathbf{X}_s)}{f_s(\mathbf{X}_s)} \cdot \frac{1}{\sqrt{2^{p-|T|}}} \prod_{t \in T} \frac{\tilde{P}_{n_t}(\mathbf{X}_t)}{f_t(\mathbf{X}_t)} \right] \quad (70)$$

$$\propto \mathbb{E} \left[\prod_{s \in S} \frac{\tilde{P}_{m_s}(\mathbf{X}_s)}{f_s(\mathbf{X}_s)} \cdot \prod_{t \in T} \frac{\tilde{P}_{n_t}(\mathbf{X}_t)}{f_t(\mathbf{X}_t)} \right] \quad (71)$$

$$\propto \mathbb{E} \left[\underbrace{\frac{\tilde{P}_{m_{s^*}}(\mathbf{X}_{s^*})}{f_{s^*}(\mathbf{X}_{s^*})}}_{u(\mathbf{X}_{s^*})} \cdot \underbrace{\prod_{s \in S \setminus \{s^*\}} \frac{\tilde{P}_{m_s}(\mathbf{X}_s)}{f_s(\mathbf{X}_s)} \cdot \prod_{t \in T} \frac{\tilde{P}_{n_t}(\mathbf{X}_t)}{f_t(\mathbf{X}_t)}}_{v(\mathbf{X}_{[p] \setminus \{s^*\}})} \right] \quad (72)$$

$$\propto \mathbb{E} \left[\frac{\tilde{P}_{m_{s^*}}(\mathbf{X}_{s^*})}{f_{s^*}(\mathbf{X}_{s^*})} \right] \cdot \mathbb{E} \left[\prod_{s \in S \setminus \{s^*\}} \frac{\tilde{P}_{m_s}(\mathbf{X}_s)}{f_s(\mathbf{X}_s)} \cdot \prod_{t \in T} \frac{\tilde{P}_{n_t}(\mathbf{X}_t)}{f_t(\mathbf{X}_t)} \right] \quad (73)$$

$$\propto \mathbb{E} \left[\frac{\tilde{P}_{m_{s^*}}(\mathbf{X}_{s^*})}{f_{s^*}(\mathbf{X}_{s^*})} \right] \quad (74)$$

$$\propto \int_{-1}^1 \frac{\tilde{P}_{m_{s^*}}(x)}{f_{s^*}(x)} f_{s^*}(x) dx \quad (75)$$

$$\propto \int_{-1}^1 \tilde{P}_{m_{s^*}}(x) dx \quad (76)$$

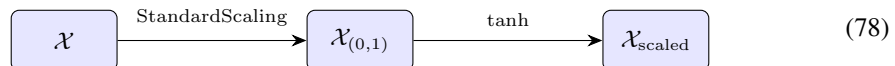
$$= 0. \quad (77)$$

□

C Our estimator in a nutshell

In this section, we detail all the computations behind our method to estimate the functional ANOVA from a mere data sample. Throughout this section, we denote by $\mathcal{X} := \{\mathbf{X}^{(i)}\}_{i=1}^n$ and $\mathcal{Y} := \{y^{(i)}\}_{i=1}^n$ the data, and $\{\mathcal{X}, \mathcal{Y}\}$ is the corresponding data sample. If in the vast majority of datasets, one can assume that the features are bounded, they rarely live natively in $[-1, 1]^p$.

Feature scaling. The first step to apply our framework on a real world dataset is a feature scaling in $[-1, 1]$. We propose to address this by first centering and reducing our data and then applying tanh to each feature. This can be described as follows:



Features are standardized to zero mean and unit variance, using the `StandardScaler` from `scikit-learn` [45].

Density estimation. We follow the procedure initially introduced by [10]. From now on, we assume that the feature sample takes values in $[-1, 1]^p$. Our theoretical guarantees depend on the true marginal densities f_S for $S \subseteq [p]$, which are unavailable in practice and must be estimated from the data. We propose to also estimate each f_S using a truncated tensorized Legendre expansion. In practice, for any $S \subseteq [p]$ and a truncation degree d_{density} , we approximate f_S as follows:

$$f_S \approx \sum_{\mathbf{m} \in \{0, \dots, d_{\text{density}}\}^{|S|}} c_S^{(\mathbf{m})} \prod_{j \in S} \tilde{P}_{m_j}, \quad (79)$$

By orthonormality of the tensorized basis, each coefficient $c_S^{(\mathbf{m})}$ is estimated as follows:

$$\hat{c}_{S,n}^{(\mathbf{m})} := \frac{1}{n} \sum_{i=1}^n \prod_{j \in S} \tilde{P}_{m_j}(\mathbf{x}_j^{(i)}). \quad (80)$$

This choice is motivated by two considerations. First, it keeps the whole pipeline fully transparent and free of additional black-box components: each coefficient reduces to an empirical average, the estimator is trained from scratch with a single hyperparameter (the truncation degree d_{density}), and it integrates seamlessly with the rest of our analysis, which is already expressed in the Legendre basis. Second, and more importantly, our goal is not to recover f_S pointwise but to enforce the hierarchical orthogonality constraint (3); since capturing a *global trend* of f_S is enough to guarantee this condition, the pointwise quality of the density estimate is largely irrelevant to our objective.

Remark C.1. In theory the number of densities to be estimated scales as $\mathcal{O}(p^K)$, but in practice we restrict ourselves to $K \in \{1, 2\}$, which keeps the estimation step tractable even in moderately high dimension.

Remark C.2 (Density clipping). In practice, we replace the raw estimate \hat{f}_S by $\max(\varepsilon, \hat{f}_S)$ (typically $\varepsilon = 10^{-2}$), in order to avoid numerical instabilities caused by regions where the estimated density is very close to zero (or negative, since the projection estimator is not constrained to be nonnegative).

Legendre polynomials are evaluated using `eval_legendre` from `SciPy` [59]. The truncation degree d_{density} and the clipping parameter ε constitute two hyperparameters of the method, referred to as `deg_density` and `density_clip` respectively.

Design matrix. With a slight abuse of notation, we still write f_S for the clipped estimated densities. We then form the *design matrix* associated with our basis functions,

$$\mathbf{B} := \left(\xi_S^{(\mathbf{m}_S)}(\mathbf{X}^{(i)}) \right)_{\substack{i \in \{1, \dots, n\} \\ (S, \mathbf{m}_S) \in \mathcal{I}_K^d}} \in \mathbb{R}^{n \times N(p, K, d)}. \quad (81)$$

The numerator of the design matrix is similarly computed via Legendre polynomials using `eval_legendre` from `SciPy`. The resulting matrix \mathbf{B} is stored as a two-dimensional NumPy array.

Linear solving. The estimator defined in (12) can now be expressed as follows:

$$\hat{\mathbf{a}}_n^{K,d} \in \underset{\beta \in \mathbb{R}^{N(p, K, d)}}{\operatorname{argmin}} \|\mathbf{B}\beta - \mathbf{y}\|_2^2, \quad \mathbf{y} := \left(\nu(\mathbf{X}^{(i)}) \right)_{1 \leq i \leq n} \in \mathbb{R}^n, \quad (82)$$

where $\|\cdot\|_2$ denotes the Euclidean norm on \mathbb{R}^n . We proceed in two stages: we first select a relevant subset of columns via a LARS procedure [16, 7], and then solve the resulting reduced system using an SVD.

Model selection is carried out using `LassoLarsIC` from `scikit-learn`, which traverses the LARS regularization path and selects the optimal support via the Bayesian Information Criterion (BIC). This yields a subset of column indices defining the reduced design matrix \mathbf{B}_{red} . The corresponding least-squares system is then solved via `numpy.linalg.lstsq` [21], which computes the minimum-norm solution through a thin SVD decomposition.

Estimator. We denote by $\hat{\nu}$ the resulting estimator, with $\hat{\nu}_S$ its component associated to each subset $S \subseteq [p]$. The full decomposition over the dataset denoted \mathbf{X}, \mathbf{y} is obtained by calling a function of the following arguments:

`K, d, d_density, density_clip, X, y.`

Remark C.3. As a final step, we recenter the resulting ANOVA components so that ν_\emptyset captures the global mean. This operation comes at negligible computational cost and merely translates the components, leaving the structure of Ξ and the hierarchical orthogonality unchanged. Prior to this step, the components were already nearly centered by construction; the residual offset is an empirical bias due to finite-sample approximation error, and correcting for it at essentially no cost is therefore worthwhile.

Remark C.4. The \tanh transformation, applied component-wise, maps the features into $[-1, 1]^p$, as required by our framework. We emphasize that this transformation is applied *solely within our explainer*: the predictive model is trained on the original data, and the baseline explainers we compare against likewise operate on the untransformed data. The comparison is therefore fair, since the underlying function of interest is identical across all methods; only its decomposition is computed in a different coordinate system.

Moreover, by uniqueness of the functional ANOVA decomposition, this change of variables leaves the importance attributions invariant. Let \mathbf{Z} denote the original features and $\mathbf{X} := \tanh(\mathbf{Z})$ the corresponding transformation with \tanh applied component-wise. Since \tanh is a bijection, the marginal structure is preserved. Let ν be the function of interest defined on the original space, with the unique decomposition

$$\nu(\mathbf{Z}) = \sum_{S \subseteq [p]} \nu_S(\mathbf{Z}_S), \quad (83)$$

and define

$$\tilde{\nu}(\mathbf{X}) := \nu(\tanh^{-1}(\mathbf{X})), \quad (84)$$

which in turn admits a unique decomposition $\tilde{\nu}(\mathbf{X}) = \sum_{S \subseteq [p]} \tilde{\nu}_S(\mathbf{X}_S)$. Substituting $\mathbf{X} = \tanh(\mathbf{Z})$ yields

$$\nu(\mathbf{Z}) = \tilde{\nu}(\tanh(\mathbf{Z})) = \sum_{S \subseteq [p]} \tilde{\nu}_S(\tanh(\mathbf{Z}_S)). \quad (85)$$

By uniqueness of this decomposition, we conclude that:

$$\forall S \subseteq [p], \quad \tilde{\nu}_S(\mathbf{X}_S) = \nu_S(\mathbf{Z}_S). \quad (86)$$

D Experiments details

D.1 Resources

All experiments were conducted on a MacBook Pro M4 with 32 GB of RAM. The code is written in Python using mainly `numpy`, `scipy`, and `scikit-learn`. All computations reduce to standard linear-algebra operations, primarily array manipulation and the resolution of linear systems and are executed on CPU.

D.2 Machine learning models

We describe the four machine learning models used in the numerical experiments of this paper. The same architectures are used consistently across all experiments, including both the analytical setting and the real-world datasets. All of these machine learning models are treated as *black boxes* by our method.

XGBoost. We use XGBoost [13], a gradient-boosted decision tree ensemble, with 100 estimators, a maximum depth of 10, and a learning rate of 0.05. Both row and column subsampling are set to 0.8 at each boosting iteration to mitigate overfitting. We use an 80/20 train-test split, with early stopping after 30 rounds without improvement on the held-out set. For classification tasks, the split is stratified and the objective is set to `binary:logistic` or `multi:softprob` depending on the number of classes; for regression, the default squared-error objective is used. The random seed is exposed as a pipeline parameter.

MLP. We use a standard feed-forward multilayer perceptron with three hidden layers of widths (128, 64, 32) and ReLU activations, followed by a dropout rate of 0.1 applied after each hidden layer. Features are standardized using a `StandardScaler` fitted on the training set. The model is trained with the Adam optimizer [29], a learning rate of 10^{-3} , a weight decay of 10^{-4} , a batch size of 256, and a maximum of 500 epochs, with early stopping after 30 epochs without improvement on the held-out validation set. The loss function is set to mean squared error for regression, binary cross-entropy with logits for two-class classification, and categorical cross-entropy otherwise. We use an 80/20 train-test split, stratified in the classification setting. The random seed is exposed as a pipeline parameter.

NAM. Neural Additive Models [1] fit a generalized additive model of the form $h(\mathbf{x}) = C + \sum_{j=1}^p h_j(\mathbf{x}_j)$, where each *shape function* h_j is parameterized by an independent univariate subnetwork. Following the standard ReLU variant of [1], each subnetwork consists of three hidden layers of widths (64, 64, 32) with ReLU activations. Features are standardized on the training set prior to training. The model is trained with the Adam optimizer [29], a learning rate of 6.74×10^{-3} decayed exponentially by a factor of 0.995 per epoch, weight decay of 10^{-6} , and an additional L_2 penalty of 10^{-3} on the shape function outputs to encourage smoothness. We use a batch size of 1024, a maximum of 1000 epochs, and early stopping after 50 epochs without improvement on the held-out validation set. The loss function is mean squared error for regression, binary cross-entropy with logits for two-class classification, and categorical cross-entropy otherwise. After training, the shape functions are centered so that each h_j has zero empirical mean over the training set, with the residual absorbed in the intercept C . We use an 80/20 train-test split, stratified in the classification setting, and the random seed is exposed as a pipeline parameter.

EBM. Explainable Boosting Machines [41] are second-order generalized additive models of the form $h(\mathbf{x}) = C + \sum_j h_j(\mathbf{x}_j) + \sum_{j,k} h_{j,k}(\mathbf{x}_j, \mathbf{x}_k)$, where each univariate and bivariate function is fitted greedily using cyclic gradient boosting with shallow decision trees. We use the reference implementation provided by the `interpret` package [41], with a maximum of 256 bins for feature discretization, 10 automatically selected pairwise interactions, and up to 5 000 boosting rounds with a learning rate of 10^{-2} . Each base learner is a shallow tree with at most 3 leaves and a minimum of 2 samples per leaf. We use an 80/20 train-test split, stratified in the classification setting. The random seed is exposed as a pipeline parameter.

D.3 Explainers

We fix in advance an evaluation set $\mathcal{X}_{\text{eval}}$ of shape $N_{\text{eval}} \times p$ on which all subsequent quantities are computed and compared. In the analytical setting, we explain the entire dataset, i.e., $N_{\text{eval}} = n = 10\,000$. For the real-world datasets, we sample $N_{\text{eval}} = 5\,000$ instances uniformly at random. For a given dataset, all methods are evaluated on the same set of instances to ensure a fair comparison.

KernelSHAP. We fix in advance a background dataset of size N_{bg} and apply the `KernelExplainer` from the `shap`³ package [36] directly to the trained model. In the analytical setting, we apply this method directly to the function ν , treated as a black box. For the real-world datasets, it is applied exclusively to the trained MLP.

DeepSHAP. We fix in advance a background dataset of size N_{bg} and apply the `DeepExplainer` from the `shap` package [36] directly to the trained model. For the real-world datasets, it is applied exclusively to the trained MLP.

³<https://github.com/shap/shap>

Remark D.1. In practice, we set $N_{\text{bg}} = 200$ for the datasets *Bike Sharing*, *California Housing* and *Pima Indians Diabetes*, a standard value in the literature. For the datasets *Adult Census Income*, *Electrical Grid Stability* and *Superconductivity*, we use $N_{\text{bg}} = 50$ for computational reasons.

TreeSHAP. We apply TreeSHAP [35], via the `TreeExplainer` class of the `shap` package, to the trained XGBoost model. We use the `tree_path_dependent` option, which computes Shapley values in the observational sense by accounting for feature dependencies through the tree structure.

TreeHFD. We apply TreeHFD [6], via the `treehfd`⁴ package, to the same trained XGBoost model as TreeSHAP. We use the first-order mode (`interaction_order=1`), which restricts the decomposition to main effects, both for computational efficiency and for consistency with our figures, in which we display the main effects.

EBM. The additive decomposition is part of the fitted EBM itself. For each evaluation instance \mathbf{x} and each feature j , the main effect $h_j(\mathbf{x}_j)$ is extracted directly via the `eval_terms` method of the `interpretML`⁵ package [41], which returns the contribution of every univariate (and bivariate) shape function to the model output. Displayed main effects are obtained by plotting $h_j(x_j)$ against x_j over the evaluation set. In the classification setting, all contributions are reported on the logit scale.

NAM. Likewise, the additive decomposition is part of the NAM architecture. For each evaluation instance \mathbf{x} and each feature j , the main effect $h_j(\mathbf{x}_j)$ is obtained by a forward pass of the j -th subnetwork on the scalar input x_j . After training, the shape functions are centered so that $\mathbb{E}[h_j(\mathbf{X}_j)] = 0$ on the training set, with the residual absorbed in the intercept C [1]. Displayed main effects are obtained as for EBM, by plotting $h_j(\mathbf{x}_j)$ against \mathbf{x}_j over the evaluation set; in classification, they are reported on the logit scale.

D.4 Analytical Case

Theoretical decomposition. In this case, we consider a random vector $\mathbf{X} \in [-1, 1]^3$ whose joint density belongs to the Farlie–Gumbel–Morgenstern [40] family and is given for $\mathbf{x} \in [-1, 1]^3$ by:

$$f_\rho(\mathbf{x}) = \frac{1}{8}(1 + \rho(\mathbf{x}_1\mathbf{x}_2 + \mathbf{x}_2\mathbf{x}_3 + \mathbf{x}_1\mathbf{x}_3)), \quad (87)$$

where $\rho \in (-\frac{1}{3}, 1)$ is the dependence parameter. The marginal densities of order 1 and 2 are explicit and are given by

$$f_j(\mathbf{x}) = \frac{1}{2}, \quad (88)$$

$$f_{i,j}(\mathbf{x}_i, \mathbf{x}_j) = \frac{1}{4}(1 + \rho \mathbf{x}_i \mathbf{x}_j), \quad (89)$$

for all $\mathbf{x}, \mathbf{x}_i, \mathbf{x}_j \in [-1, 1]$. Each marginal is uniform on $[-1, 1]$, and the pairwise correlation satisfies $\text{Corr}(\mathbf{X}_i, \mathbf{X}_j) = \rho/3$ for all $i \neq j$. Note that for any $\rho \in (-1/3, 1)$, we have:

$$0 < \underbrace{\frac{1}{8}(1 - \rho)}_{c_1} \leq f_\rho \leq \underbrace{\frac{1}{8}(1 + 3\rho)}_{c_2} < \infty, \quad (90)$$

which satisfies the Assumption 3.1. We define the theoretical components of ν in terms of elements of Ξ as follows:

$$\nu_1(\mathbf{x}_1) := \frac{\sqrt{\frac{2}{7}} \tilde{P}_3(\mathbf{x}_1) - \sqrt{\frac{2}{3}} \tilde{P}_1(\mathbf{x}_1)}{f_1(\mathbf{x}_1)}, \quad (91)$$

$$\nu_2(\mathbf{x}_2) := \frac{\sqrt{\frac{2}{3}} \tilde{P}_1(\mathbf{x}_2) + \sqrt{\frac{2}{5}} \tilde{P}_2(\mathbf{x}_2)}{f_2(\mathbf{x}_2)}, \quad (92)$$

$$\nu_{1,2}(\mathbf{x}_1, \mathbf{x}_2) := \frac{\frac{2}{9} \tilde{P}_4(\mathbf{x}_1) \tilde{P}_4(\mathbf{x}_2) + \frac{2}{17} \tilde{P}_8(\mathbf{x}_1) \tilde{P}_8(\mathbf{x}_2)}{f_{1,2}(\mathbf{x}_1, \mathbf{x}_2)}, \quad (93)$$

and $\nu_\emptyset = \nu_3 = \nu_{1,3} = \nu_{2,3} = \nu_{1,2,3} = 0$.

⁴<https://github.com/ThalesGroup/treehfd>

⁵<https://interpret.ml/>

Simulations. In our theoretical setup, the function ν is available in closed form, and samples of \mathbf{X} can be drawn via rejection sampling from the uniform distribution on $[-1, 1]^3$ using the density f_ρ . We set $\rho = 1/2$ for simplicity. The illustration in Fig 7 is produced with $n = 10\,000$ samples.

Comparisons. We compare the main effects ν_1, ν_2, ν_3 against several explanation methods (KernelSHAP, TreeSHAP, TreeHFD) and interpretable models (NAM and EBM). In each case, we follow the procedure described above and explain the 10 000 instances of the dataset.

- **KernelSHAP.** We apply KernelSHAP directly to ν , treated as a *black-box* model.
- **TreeSHAP.** We train an XGBoost model and apply TreeSHAP to the trained estimator.
- **TreeHFD.** We apply TreeHFD to the same XGBoost model.
- **NAM.** We train a NAM and report its learned main effects.
- **EBM.** We train an EBM and report its learned main effects.

Remark D.2. Note that we apply our own estimator on this synthetic dataset, assuming that the theoretical ν is black-box. And we verify that our method also captures the true underlying ANOVA structure (see Fig.8).

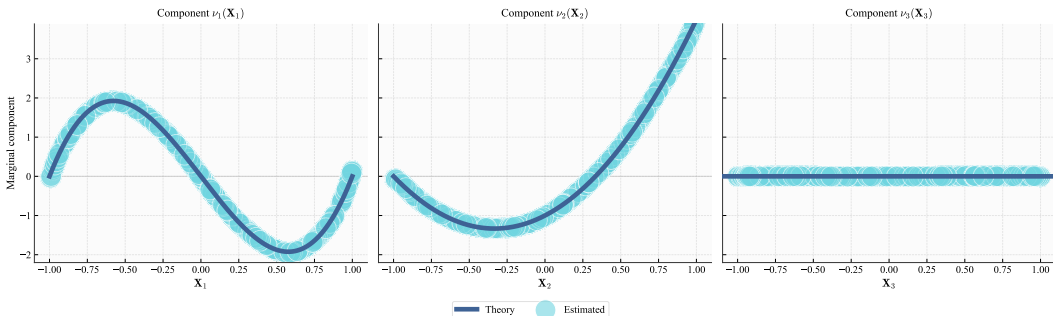


Figure 8: Estimated main effects in the analytical setting for X_1 , X_2 , and the irrelevant variable X_3 . We take $K = 2$, $d = 10$, $d_{\text{density}} = 10$ and $\varepsilon = 0.01$

D.5 Datasets

The *California Housing* dataset is directly available from `scikit-learn`. The remaining datasets are retrieved from the UCI Machine Learning Repository [15] using the `fetch_ucirepo` function of the `ucimlrepo`⁶ package. All features are used for every dataset, with the exception of *Bike Sharing*, where we retain only eight: `hr`, `weekday`, `holiday`, `season`, `atemp`, `hum`, `windspeed`, and `weathersit` following [6].

D.6 Hyperparameters

In this section, we specify the hyperparameters used by our method on each dataset. Recall that these hyperparameters are:

1. K : the truncation order of the interaction levels;
2. d : the maximum polynomial degree (numerator);
3. d_{density} : the maximum polynomial degree used to estimate the marginal densities (denominator);
4. ε : the clipping threshold applied to the estimated densities.

Remark D.3. In practice, we always take $K \in \{1, 2\}$, so that our method reduces to a GAM ($K = 1$) or a GA^2M ($K = 2$). The density-estimation degree d_{density} can also be kept small: a low-degree polynomial is typically sufficient to capture the overall *trend* of the marginal densities. Finally, we never go beyond $d = 10$ for the shape-function polynomials, as we empirically observe no additional

⁶<https://pypi.org/project/ucimlrepo/>

Table 4: Hyperparameters of our method for all models across all datasets. The – entries correspond to datasets on which the NAM baseline was not trained for computational reasons.

ID	XGBoost				MLP				EBM				NAM			
	K	d	d_{density}	ε	K	d	d_{density}	ε	K	d	d_{density}	ε	K	d	d_{density}	ε
BS	2	10	5	0.01	2	8	6	0.01	2	10	4	0.01	–	–	–	–
CH	2	10	4	0.01	1	10	4	0.01	2	10	4	0.01	1	10	4	0.01
CI	1	10	4	0.01	1	10	4	0.01	1	10	6	0.01	–	–	–	–
EG	2	4	4	0.01	2	4	4	0.01	2	4	4	0.01	1	4	4	0.01
PI	2	5	4	0.1	2	5	4	0.01	2	5	4	0.01	1	10	4	0.01
SC	1	10	10	0.01	1	10	10	0.01	1	10	10	0.01	–	–	–	–

signal capture beyond this degree. Pushing d further can even degrade the hierarchical orthogonality of the decomposition, a signal that either a more sophisticated penalized model selection scheme or an increase of the truncation order to $K = 3$ would be required.

D.7 Performance metrics

In this subsection, we report all performance metrics that were omitted from the main body of the paper.

Tables. For clarity, we reproduce here the tables reporting the dataset characteristics and the performance of our method across the four models and all datasets. Tab 5 and Tab 6 report the predictive performance of the trained models on the six real-world datasets, together with the corresponding metrics of our method.

Table 5: Dataset characteristics and performance of our method.

ID	n	p	XGB				MLP			
			Perf	K	R^2	MaxCorr	Perf	K	R^2	MaxCorr
BS	17 379	8	0.86	2	0.92	9.49e−2	0.85	2	0.91	8.83e−2
CH	20 640	8	0.84	2	0.86	6.35e−2	0.81	1	0.88	0.00
CI	48 842	14	0.88	1	0.91	0.00	0.85	1	0.94	0.00
EG	10 000	12	0.93	2	0.89	7.41e−3	0.98	2	0.95	6.61e−3
PI	768	8	0.74	2	0.85	9.56e−2	0.73	2	0.99	0.00
SC	21 263	81	0.93	1	0.86	0.00	0.91	1	0.89	0.00

Table 6: Dataset characteristics and performance of our method on EBM and NAM.

ID	n	p	EBM				NAM			
			Perf	K	R^2	MaxCorr	Perf	K	R^2	MaxCorr
BS	17 379	8	0.83	2	0.96	9.52e−2	–	–	–	–
CH	20 640	8	0.83	2	0.89	4.04e−2	0.76	1	0.94	0.00
CI	48 842	14	0.88	1	0.90	0.00	–	–	–	–
EG	10 000	12	0.94	2	0.99	5.58e−3	0.88	1	1.00	0.00
PI	768	8	0.76	2	0.97	0.00	0.73	1	1.00	0.00
SC	21 263	81	0.90	1	0.88	0.00	–	–	–	–

Perf denotes the predictive performance of the trained model: classification accuracy for classification tasks and the coefficient of determination for regression tasks. The quantity R^2 is the reconstruction coefficient of determination of our estimator, i.e. the fraction of the output variance captured by our decomposition on the entire dataset. Finally, MaxCorr is defined as

$$\text{MaxCorr} := \max_{(S,T) \in \mathcal{A}} |\mathbb{E}[\hat{\nu}_S(\mathbf{X}_S) \hat{\nu}_T(\mathbf{X}_T)]| \cdot (\mathbb{E}[\hat{\nu}_S(\mathbf{X}_S)^2] \mathbb{E}[\hat{\nu}_T(\mathbf{X}_T)^2])^{-1/2}, \quad (94)$$

where $\mathcal{A} = \{(S, T) : T \subsetneq S, \mathbb{V}(\widehat{\nu}_S(\mathbf{X}_S))/\mathbb{V}(\nu(\mathbf{X})) \geq 1\%\}$. We restrict the maximum to interaction components whose variance represents at least 1% of the output variance (following [6]), so as to discard components with negligible contribution to the decomposition.

Computation time. The computation times of our method on each real-world dataset are reported in Tab. 2. For each dataset, we fix the random seed to 42 and train the corresponding machine learning model. We then apply our decomposition method to each trained model over 10 independent runs, and report the mean and standard deviation. We observe that our method is extremely fast, enabling the explanation of hundreds or thousands of instances in a few seconds or less. For instance, the quasi-additive structure of an MLP trained on the *Adult Census Income* dataset allows us to explain all 48 842 instances in approximately 0.6 s.

Hierarchical orthogonality. As a consequence of the hierarchical orthogonality constraint (3), the components $\{\nu_S(\mathbf{X}_S)\}_{S \subseteq [p]}$ must satisfy

$$\forall S, T \subseteq [p], \quad T \subsetneq S \implies \mathbb{E}[\nu_S(\mathbf{X}_S) \nu_T(\mathbf{X}_T)] = 0. \quad (95)$$

In practice, we measure the empirical cosine between pairs of components ν_S and ν_T with $T \subsetneq S \subseteq [p]$. When $T = \emptyset$, the cosine is defined by:

$$\frac{\mathbb{E}[\nu_S(\mathbf{X}_S)]}{\sqrt{\mathbb{E}[\nu_S(\mathbf{X}_S)^2]}}, \quad (96)$$

which quantifies the degree of centering of ν_S . For $T \neq \emptyset$, we compute

$$\frac{\mathbb{E}[\nu_S(\mathbf{X}_S) \nu_T(\mathbf{X}_T)]}{\sqrt{\mathbb{E}[\nu_S(\mathbf{X}_S)^2] \mathbb{E}[\nu_T(\mathbf{X}_T)^2]}}. \quad (97)$$

After estimation, we systematically recenter the estimated components $\widehat{\nu}_S$, so that for every $S \subseteq [p]$,

$$\frac{\mathbb{E}[\widehat{\nu}_S(\mathbf{X}_S)]}{\sqrt{\mathbb{E}[\widehat{\nu}_S(\mathbf{X}_S)^2]}} = 0. \quad (98)$$

As a result, for every $\emptyset \subsetneq T \subsetneq S \subseteq [p]$, the empirical cosine between $\widehat{\nu}_S$ and $\widehat{\nu}_T$ coincides with their empirical correlation, since both components are centered. Naturally, MaxCorr is computed from this quantity.

Remark D.4. Although the theoretical decomposition provably satisfies the constraint (3), exact hierarchical orthogonality is difficult to achieve in practice, especially on finite samples combined with imperfect density estimation.

For the analytical setting, we report in Tab 7 the empirical cosines, in absolute value, between the theoretical ANOVA components. The hierarchical orthogonality constraint is well satisfied in this case: all corresponding cosines are below 10^{-2} , confirming numerically the theoretical result.

Table 7: Empirical cosines between theoretical ANOVA components on the analytical setting, reported as mean \pm standard deviation over 100 independent runs with $n = 100\,000$ samples each.

(S, T)	Absolute cosine
$(\{1\}, \emptyset)$	0.0027 ± 0.0018
$(\{2\}, \emptyset)$	0.0026 ± 0.0019
$(\{1, 2\}, \emptyset)$	0.0024 ± 0.0020
$(\{1, 2\}, \{1\})$	0.0022 ± 0.0017
$(\{1, 2\}, \{2\})$	0.0028 ± 0.0024

Explained variance. Across all experiments, the trained models prove to be highly additive, which explains the consistently high R^2 values reported in Tab 3 and Tab 6. However, our decomposition does not achieve a perfectly unitary R^2 , for three reasons. *First*, the truncated decomposition is restricted to interaction orders $K \in \{1, 2\}$ and therefore cannot capture signal carried by higher-order interactions, whenever the underlying model exhibits them. *Second*, our estimator can still be

refined: a more accurate density estimator or a more sophisticated (*e.g.*, penalized) strategy for the regularized least-squares problem would improve the fraction of variance recovered. *Third*, and more fundamentally, recovering exactly 100% of the variance is not a desirable target for an explainability method. Methods that enforce the *efficiency* axiom by construction, such as the SHAP family, distribute the totality of the prediction over feature attributions. This is visible in our experiments: SHAP-based estimates produce substantially noisy curves. By relaxing the efficiency requirement, our approach forgoes explaining the last few percent of variance in exchange for attributions that track the genuine additive structure of the signal rather than its residual noise.

D.8 Additional Analytical Case

We provide a supplementary analytical example in an unbounded-density setting, where Assumption 3.1 no longer holds. We observe that the results of this experiment are keeping relevant. Let consider $\mathbf{X} \in [-1, 1]^3$ with $\mathbf{X}_j := \tanh(\mathbf{Z}_j)$ for $j \in [3]$, where $\mathbf{Z} \sim \mathcal{N}(\mathbf{0}, \Sigma)$ and Σ has unit diagonal and constant off-diagonal $\rho > 0$. The marginal densities are

$$f_j(x) = \frac{1}{\sqrt{2\pi}(1-x^2)} \exp\left(-\frac{1}{2}\sigma^2(x)\right), \quad (99)$$

$$f_{i,j}(x_i, x_j) = \frac{1}{2\pi\sqrt{1-\rho^2}(1-x_i^2)(1-x_j^2)} \times \exp\left(-\frac{\sigma^2(x_i) - 2\rho\sigma(x_i)\sigma(x_j) + \sigma^2(x_j)}{2(1-\rho^2)}\right), \quad (100)$$

where $\sigma := \operatorname{arctanh}$. The theoretical ANOVA components are defined as in the first analytical case; only the denominators change due to the different densities. We set $\rho = 1/2$ and draw samples by generating $\mathbf{Z}^{(1)}, \dots, \mathbf{Z}^{(n)}$ i.i.d. $\mathcal{N}(\mathbf{0}, \Sigma)$ and applying \tanh coordinate-wise.

Fig 9 shows the estimated main effects with $n = 10\,000$ samples: all methods closely track the theoretical components on \mathbf{X}_1 and \mathbf{X}_2 , and correctly assign near-zero contribution to \mathbf{X}_3 . Fig 10 displays the comparison with our estimator, treating ν as a black box. Finally, Tab 8 reports the empirical cosines between ANOVA components, confirming that hierarchical orthogonality holds empirically despite the violation of Assumption 3.1.

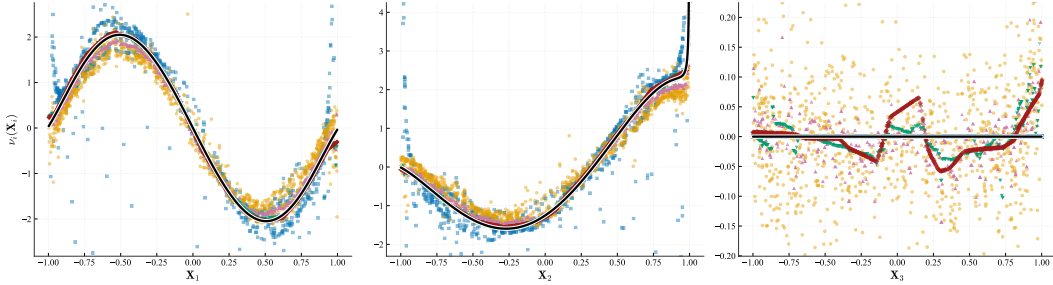


Figure 9: Estimated main effects in the unbounded-density setting for \mathbf{X}_1 , \mathbf{X}_2 and \mathbf{X}_3 . Comparison with KernelSHAP, TreeSHAP, TreeHFD, NAM and EBM.

Table 8: Empirical cosines between theoretical ANOVA components in the unbounded-density setting (mean \pm std over 100 runs, $n = 100\,000$).

(S, T)	Absolute cosine
$(\{1\}, \emptyset)$	0.0023 ± 0.0017
$(\{2\}, \emptyset)$	0.0025 ± 0.0019
$(\{1, 2\}, \emptyset)$	0.0033 ± 0.0020
$(\{1, 2\}, \{1\})$	0.0017 ± 0.0013
$(\{1, 2\}, \{2\})$	0.0087 ± 0.0132

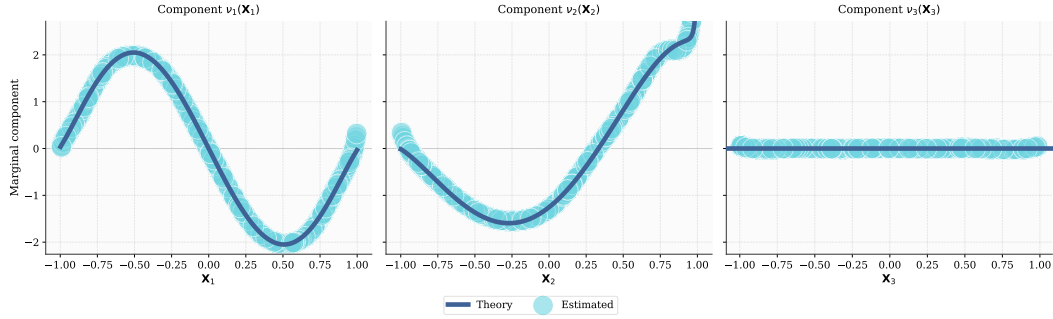


Figure 10: Comparison between the theoretical ANOVA components and our estimator ($K = 2$, $d = 10$, $d_{\text{density}} = 10$, $\varepsilon = 0.01$) in the unbounded-density setting.

E Additional Figures

E.1 Bike Sharing Dataset

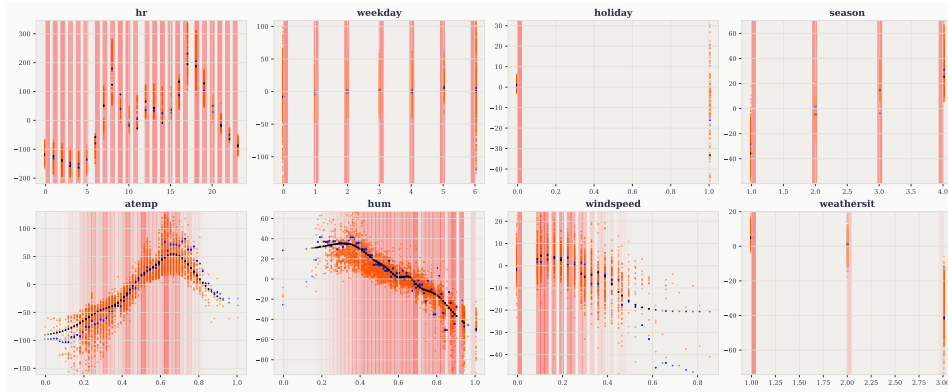


Figure 11: Estimated main effects on *Bike Sharing*: our method (black) vs [TreeHFD \(main effects\)](#) and [TreeSHAP](#) on a trained XGB.

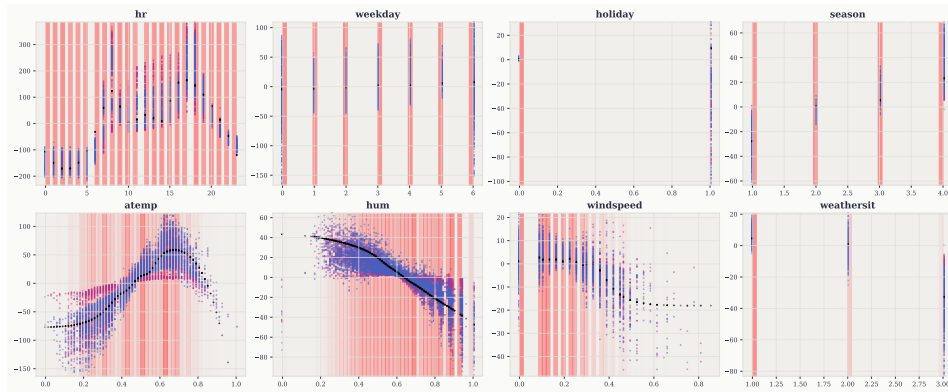


Figure 12: Estimated main effects on *Bike Sharing*: our method (black) vs [KernelSHAP](#) and [DeepSHAP](#) on a trained MLP.

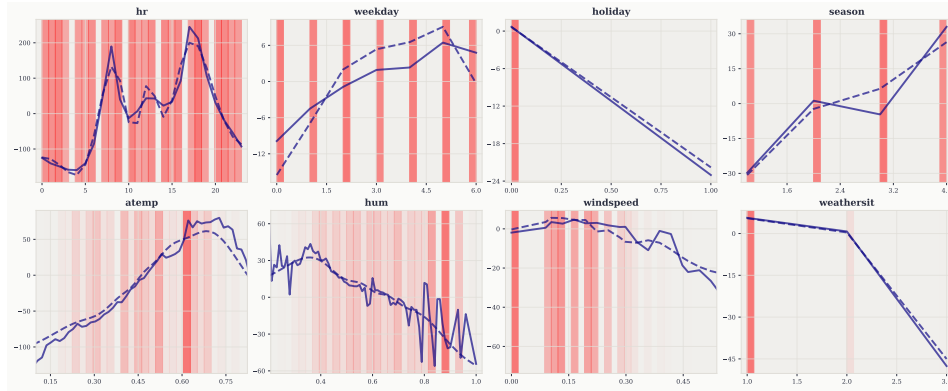


Figure 13: Comparison of native main effects from an EBM with those recovered by our method on *Bike Sharing*. EBM (solid) vs our method (dashed).

E.2 California Housing Dataset

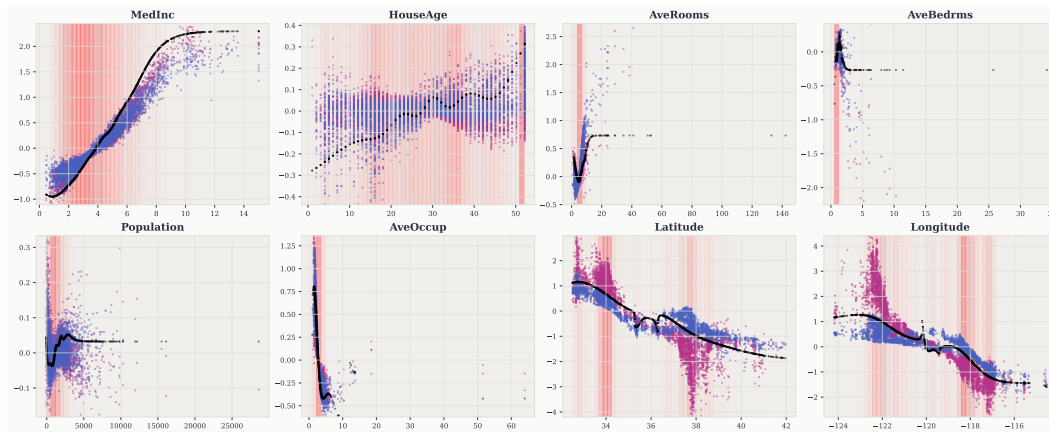


Figure 14: Estimated main effects on *California Housing*: our method (black) vs KernelSHAP and DeepSHAP on a trained MLP.

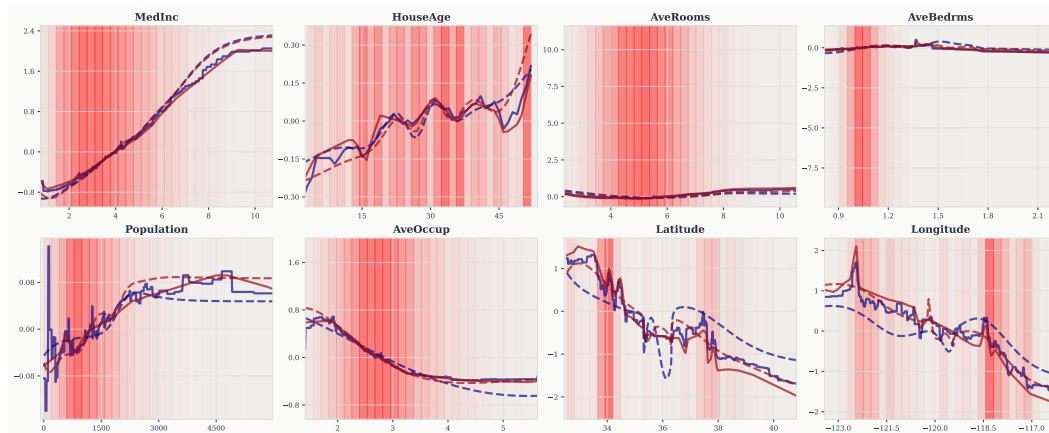


Figure 15: Comparison of native main effects from an EBM with those recovered by our method on *California Housing*. EBM (solid) vs our method (dashed); NAM (solid) vs our method (dashed).

E.3 Census Income Dataset

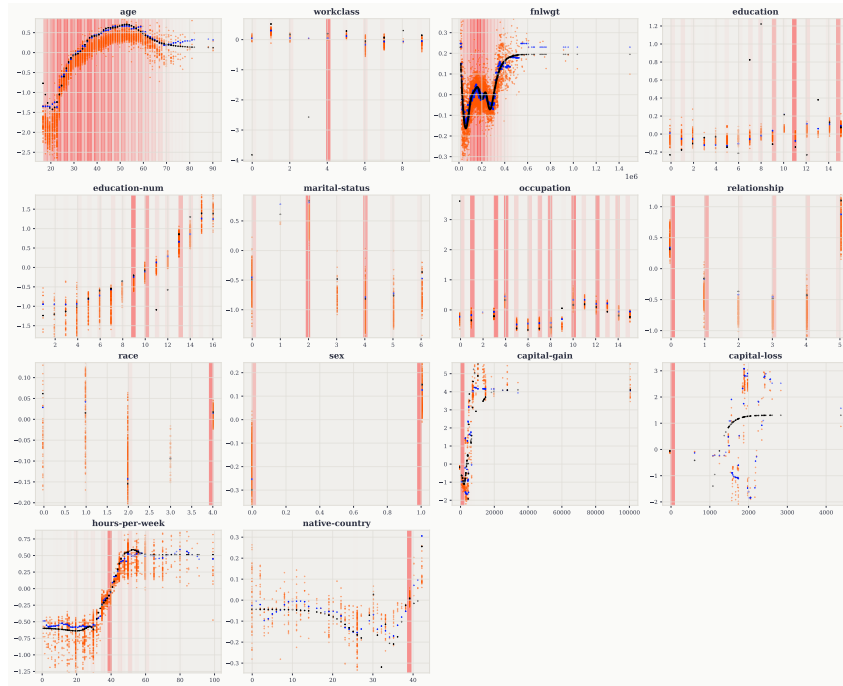


Figure 16: Estimated main effects on *Census Income*: our method (black) vs [TreeHFD \(main effects\)](#) and [TreeSHAP](#) on a trained XGB.

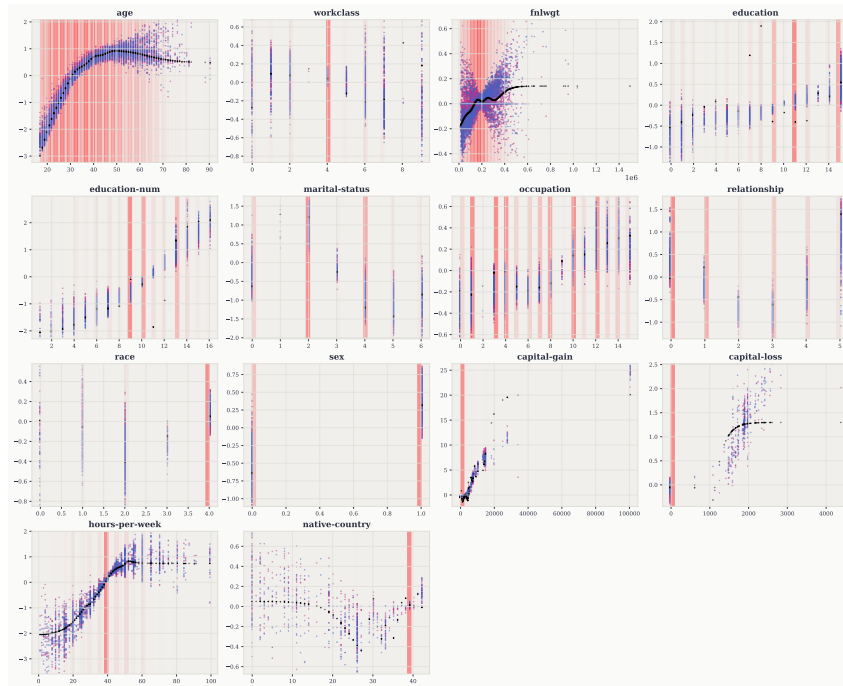


Figure 17: Estimated main effects on *Census Income*: our method (black) vs [KernelSHAP](#) and [DeepSHAP](#) on a trained MLP.

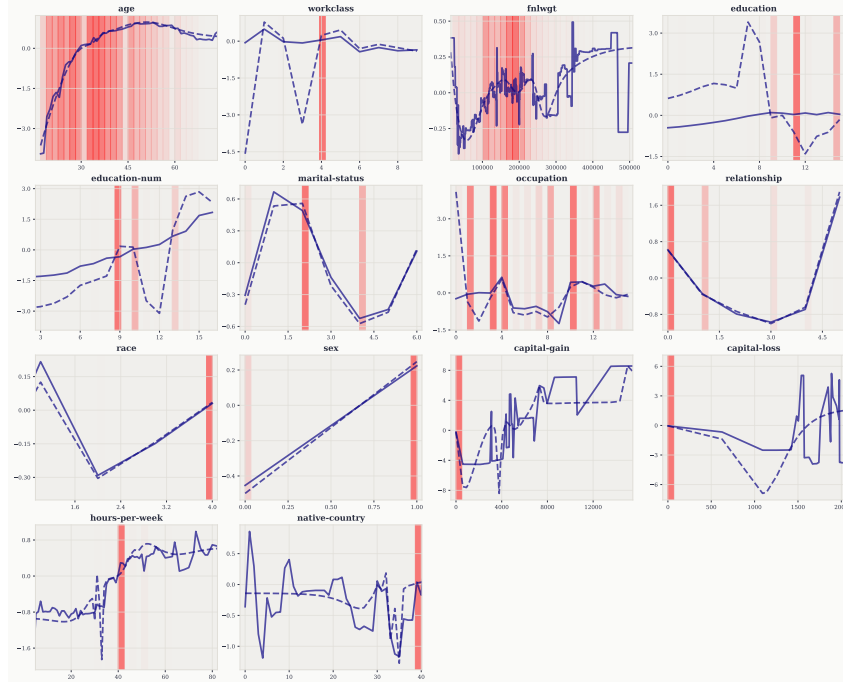


Figure 18: Comparison of native main effects from an EBM with those recovered by our method on *Census Income*. EBM (solid) vs our method (dashed).

E.4 Electrical Grid Dataset

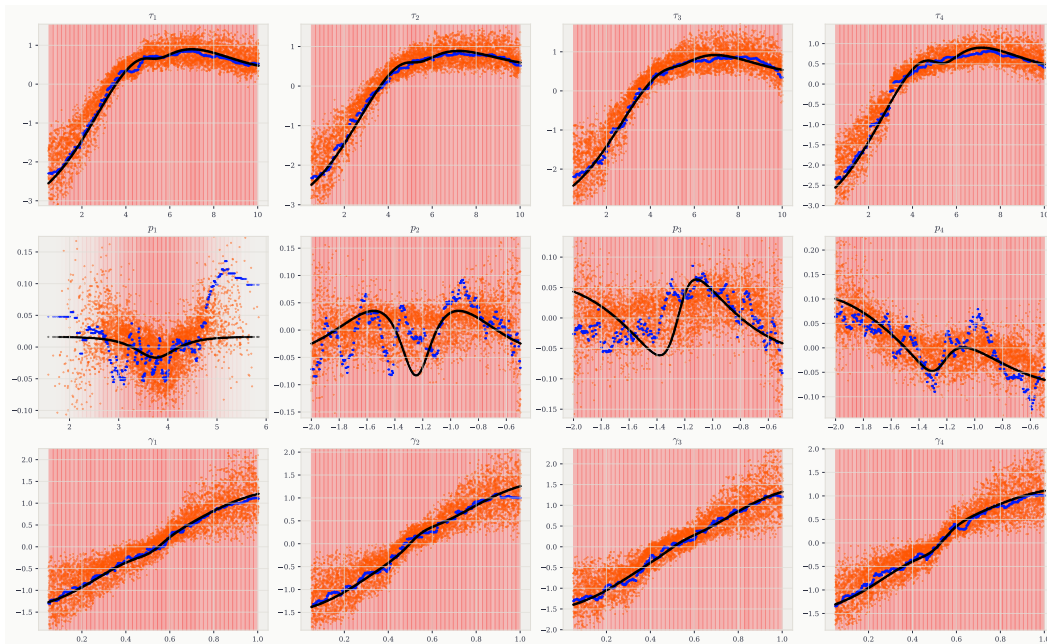


Figure 19: Estimated main effects on *Electrical Grid*: our method (black) vs TreeHFD (main effects) and TreeSHAP on a trained XGB.

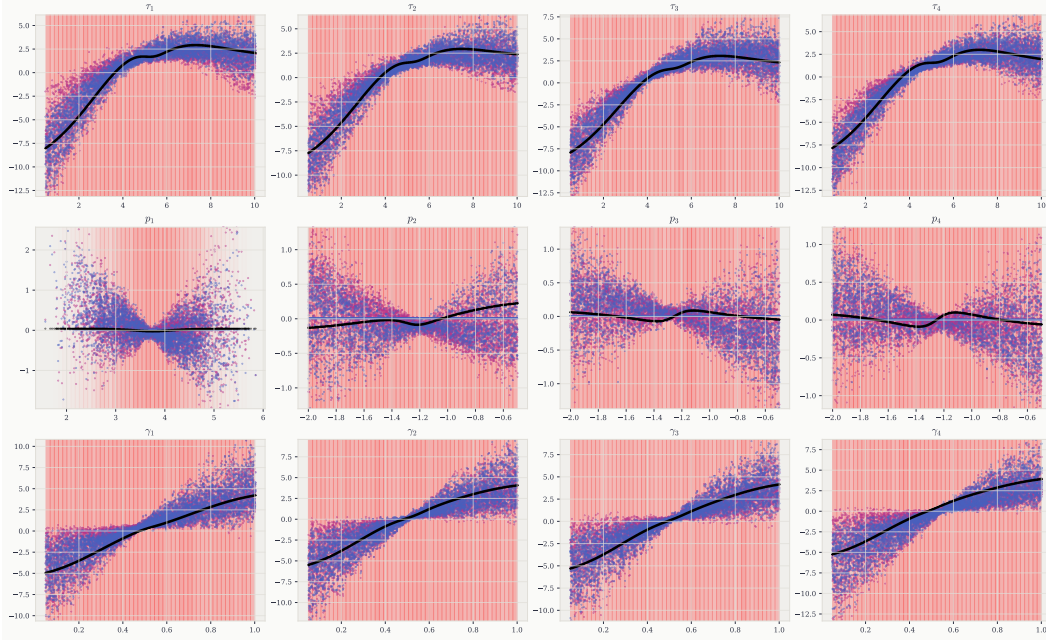


Figure 20: Estimated main effects on *Electrical Grid*: our method (black) vs KernelSHAP and DeepSHAP on a trained MLP.

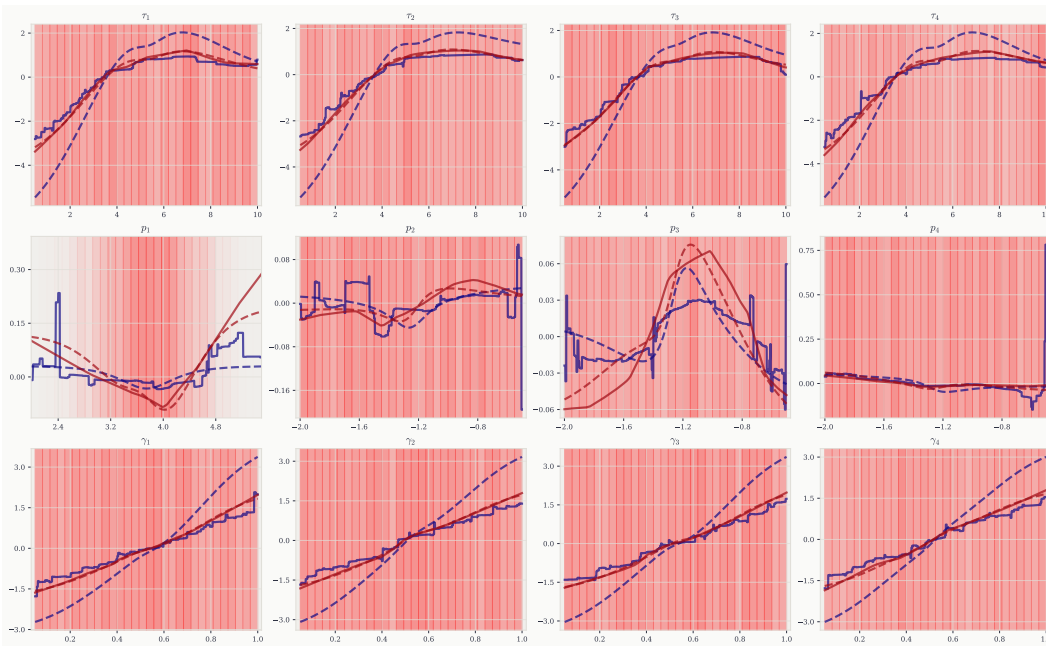


Figure 21: Comparison of native main effects from an EBM with those recovered by our method on *Electrical Grid*. EBM (solid) vs our method (dashed); NAM (solid) vs our method (dashed).

E.5 Diabetes Dataset

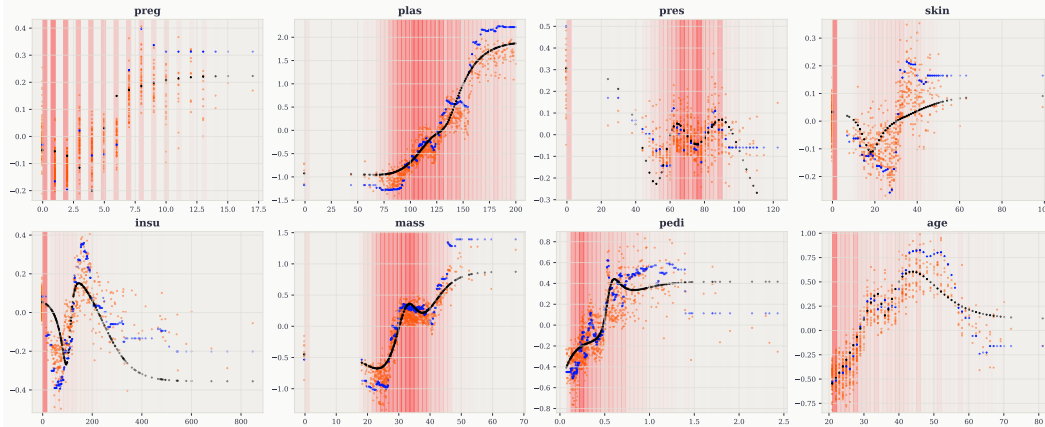


Figure 22: Estimated main effects on *Diabetes*: our method (black) vs [TreeHFD](#) (main effects) and [TreeSHAP](#) on a trained XGB.

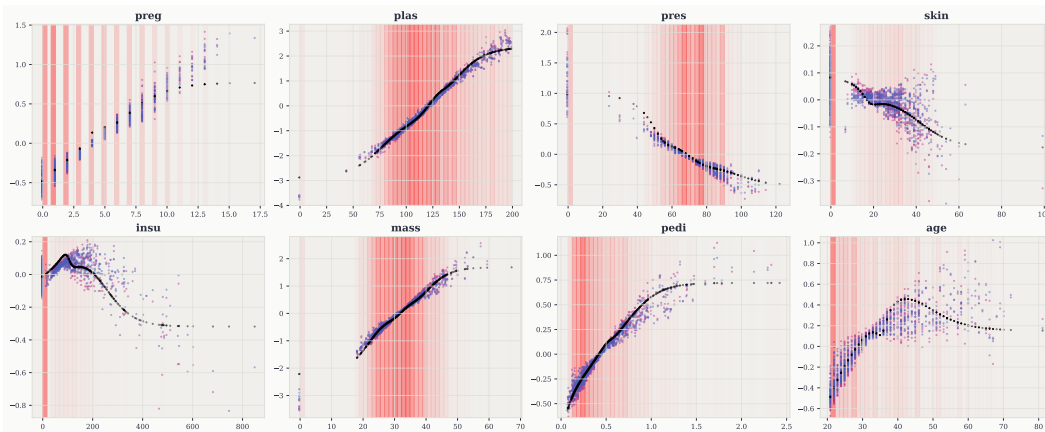


Figure 23: Estimated main effects on *Diabetes*: our method (black) vs [KernelSHAP](#) and [DeepSHAP](#) on a trained MLP.

F Limitations

In this section, we detail all the limitations related to our work. These limitations also open potential new problems and interesting future work.

Curse of dimensionality. Since the functional ANOVA expands a function $\nu(\mathbf{X})$ in 2^p components, it intrinsically suffers from the well-known *curse of dimensionality*. This said, this limitation is common to a lot of post-hoc explanation methods and interpretable models. Furthermore, this limitation is theoretical but in practice, one may rely on the sparsity of the decomposition. In practice, we restrict to low interaction order and truncate the polynomials degrees but we could also introduce a more general regularization problem.

Regularization. The theoretical penalized optimization problem is given by:

$$\operatorname{argmin}_{\beta} \left\{ \left\| \nu(\mathbf{X}) - \sum_{S \subseteq [p]} \sum_{\mathbf{m}_S \in \mathbb{N}_+^{|S|}} \beta_S^{(\mathbf{m}_S)} \cdot \xi_S^{(\mathbf{m}_S)}(\mathbf{X}) \right\|_{L^2} + \Omega(\beta) \right\}, \quad (101)$$

where $\Omega(\cdot)$ is a penalization term to define. A natural extension of our work, first in the bounded setting then in the general case, would be finding an optimal $\Omega(\cdot)$ and then solving this problem without relying on truncations. However, we acknowledge that it is a non trivial extension of our work and that truncating on interaction order and polynomial degrees is natural and widely used in practice.

Support assumption. We acknowledge that all theoretical results and experiments are presented on $[-1, 1]^p$ for simplicity; this is without loss of generality, as the construction extends to any compact domain $[a_1, b_1] \times \dots \times [a_p, b_p]$ by an affine rescaling of the Legendre polynomials. At the end, we can assume that \mathbf{X} takes values in a hyperrectangle and has a probability density function f with respect to the Lebesgue measure λ and such that $0 < c_1 \leq f \leq c_2 < \infty$. This assumption is widely used in the literature and in practice we can assume that data are bounded (or one can apply a transformation to bound them) but we acknowledge that it is at least a theoretical limitation. Extending the framework beyond bounded continuous distributions is a natural but non-trivial challenge: it would require replacing the Legendre basis with an appropriate orthogonal family and the convergence properties of the resulting series would need to be carefully established. Handling mixed continuous-categorical inputs raises additional structural questions, as the decomposition would need to combine polynomial expansions with discrete summation over categorical levels while still being a basis.

Our proposed pipeline. The proposed two-stage estimation procedure is deliberately elementary and, as demonstrated, performs reliably across our benchmark experiments. Nevertheless, several aspects of the pipeline leave room for further refinement. First, our reference implementation is written in pure Python and executed on CPU, prioritizing clarity over performance; a GPU-accelerated implementation, together with vectorization and the use of compiled backends, would likely yield substantial speed-ups and enable scaling to higher dimensions. Second, the first stage relies on density estimation: more expressive alternatives—such as kernel density estimators with adaptive bandwidth selection, Gaussian mixture models, or normalizing flows—could better capture the signal and improve the hierarchical orthogonality. Finally, the second stage reduces to solving a linear system, for which tailored iterative solvers, preconditioning strategies, or low-rank approximations could substantially reduce the computational cost; the optimal choice, however, is tied to the regularization strategy, which is itself a limitation and a natural direction for future work.